ARTIFICIAL NEURAL NETWORK-BASED DESIGN TOOL FOR THE HORIZONTAL STABILIZER OF A HELICOPTER

BİR HELİKOPTER YATAY DENGELEYİCİSİ İÇİN YAPAY SİNİR AĞI TABANLI TASARIM ARACI

EREN DUZCU

PROF. DR. BORA YILDIRIM

Supervisor

Submitted to Graduate School of Science and Engineering of Hacettepe University

as a Partial Fulfillment to the Requirements

for the Award of the Degree of Master of Sciences

in Mechanical Engineering

2022

ABSTRACT

ARTIFICIAL NEURAL NETWORK-BASED DESIGN TOOL FOR THE HORIZONTAL STABILIZER OF A HELICOPTER

Eren DUZCU

Master of Sciences, Department of Mechanical Engineering

Supervisor: Prof. Dr. Bora YILDIRIM

December 2022, 75 pages

Designing a helicopter is quite difficult and complex. Every decision made in the preliminary design phase seriously impacts the further design phases of a helicopter project. Therefore, it is vital to initially make the right and logical decisions for the design. Hand calculations, finite element analyses, and structural tests are beneficial to determine the conceptual design parameters. However, it takes much time to perform many finite element analyses and hand calculations. Furthermore, testing different types of structures in the early design stages can be very costly. These time-consuming and expensive processes are repeated in the structural design stage of each various project. Therefore, an efficient solution is needed to address this problem. Artificial neural networks are powerful models that may be used to overcome this issue and to reduce the effort and time spent in the initial design phase. In this thesis, an artificial neural network-based

design tool has been developed to determine the static structural characteristics of the horizontal stabilizer of a helicopter. The database required for training an artificial neural network model was created utilizing the finite element analyses of the horizontal stabilizer. These analyses were performed under the aerodynamic load for different design variables. The neural network model trained with this data was built in Python using the Keras library. The model outputs were then compared with the finite element analysis results, and the model performance was presented. Lastly, the database was reduced using the Hammersley sampling methodology, and the effect of decreasing the number of data feeding the network model was evaluated.

ÖZET

BİR HELİKOPTER YATAY DENGELEYİCİSİ İÇİN YAPAY SİNİR AĞI TABANLI TASARIM ARACI

Eren DUZCU

Yüksek Lisans, Makina Mühendisliği Bölümü

Tez Danışmanı: Prof. Dr. Bora YILDIRIM

Aralık 2022, 75 sayfa

Helikopter tasarlamak oldukça zor ve karmaşıktır. Ön tasarım aşamasında verilen her karar, helikopter projesinin sonraki tasarım aşamalarını ciddi şekilde etkiler. Bu nedenle tasarım için başlangıçta doğru ve mantıklı kararların verilmesi hayati önem taşımaktadır. El hesaplamaları, sonlu eleman analizleri ve yapısal testler kavramsal tasarım parametrelerinin belirlenmesinde faydalıdır. Ancak, sonlu elemanlar analizleri yapmak ve el hesabı yapmak oldukça fazla zaman alır. Ayrıca, erken tasarım aşamalarında farklı yapı tiplerini test etmek çok maliyetli olabilir. Bu zaman alıcı ve pahalı süreçler, her farklı projenin yapısal tasarım aşamasında tekrarlanır. Bu nedenle, bu sorunu çözmek için etkili bir çözüme ihtiyaç vardır. Yapay sinir ağları, bu sorunu aşmak ve ilk tasarım aşamasında harcanan emek ve zamanı azaltmak için kullanılabilecek güçlü modellerdir. Bu tez çalışmasında, bir helikopterin yatay stabilizatörünün statik yapısal özelliklerini belirlemek için yapay sinir ağı tabanlı bir tasarım aracı geliştirilmiştir. Bir yapay sinir ağı

modelinin eğitimi için gerekli olan veri tabanı, yatay dengeleyicinin sonlu elemanlar analizlerinden yararlanılarak oluşturulmuştur. Bu analizler, farklı tasarım değişkenleri için aerodinamik yük altında gerçekleştirilmiştir. Bu verilerle eğitilen sinir ağı modeli Python'da Keras kütüphanesi kullanılarak oluşturulmuştur. Model çıktıları daha sonra sonlu elemanlar analizi sonuçları ile karşılaştırılmış ve model performansı sunulmuştur. Son olarak, Hammersley örnekleme metodolojisi kullanılarak veri tabanı azaltılmış ve ağ modelini besleyen veri sayısını azaltmanın etkisi değerlendirilmiştir.

Anahtar Kelimeler: Bir Helikopterin Yatay Dengeleyicisi, Sonlu Elemanlar Analizi, Yapay Sinir Ağları, Deney Tasarımı

ACKNOWLEDGEMENTS

TABLE OF CONTENTS

LIST OF FIGURES

LIST OF TABLES

SYMBOLS AND ABBREVIATIONS

Abbreviations

AI   Artificial Intelligence

Adam   Adaptive Moment Estimation

ANN   Artificial Neural Network

CFD   Computational Fluid Dynamics

DOE   Design of Experiments

FE   Finite Element

FEA   Finite Element Analysis

FEM   Finite Element Method

LHS   Latin Hypercube Sampling

MLP   Multilayer Perceptron

MSE   Mean Squared Error

NN   Neural Network

ReLU   Rectified Linear Unit

RMSprop   Root Mean Square Propagation

SCF   Stress Concentration Factor

SGD   Stochastic Gradient Descent

TRT   Total Rotor Thrust

Symbols

α The Learning Rate

β The Exponential Decay Rate Parameter

b_k	Bias
E	Young's Modulus
φ	Activation Function
F_{tu}	Tensile Ultimate Stress
F_{ty}	Tensile Yield Stress
F_{cy}	Compressive Yield Stress
g_t	The Gradient of the Objective Function
m_t, v_t	Exponentially Weighted Averages
T_x	Translation in the X Direction
T_y	Translation in the Y Direction
T_z	Translation in the Z Direction
v	Poisson's Ratio
x_j	Input Signals
w_{kj}	Synaptic Weights
y_k	Output of the Neural Network Model

1. INTRODUCTION

It is quite challenging and complicated to design a helicopter. The decisions made in the preliminary design stage significantly affect the further design stages of a helicopter project. As the design phase progresses, the knowledge about the design increases. In contrast, the initial design freedom becomes restricted as the design matures, as illustrated in Figure 1.1. Therefore, it is crucial to make the right and logical decisions for the design in the initial phase.
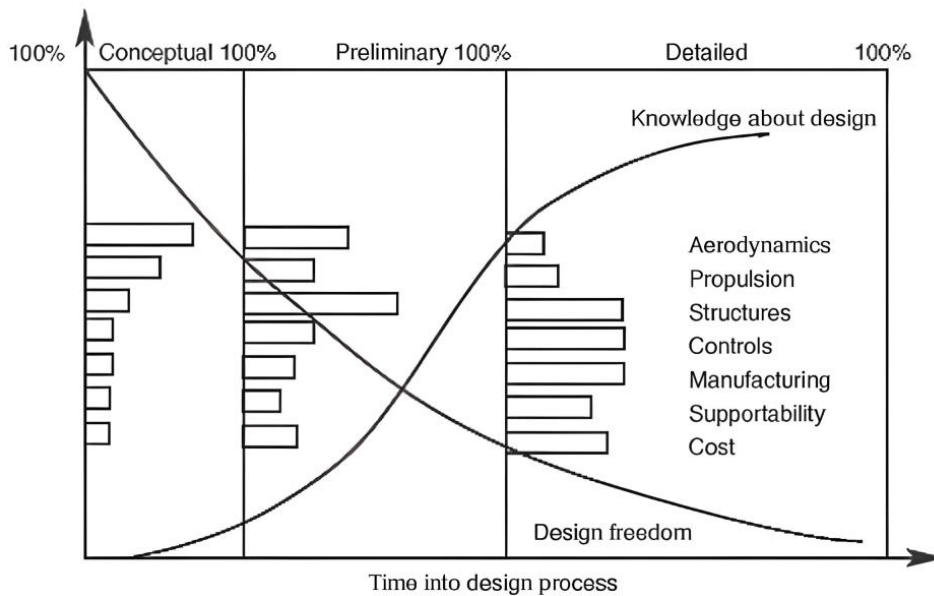
Figure 1.1 Design Progression [1]

Especially the structural design parameters that are determined in the initial phase can cause a problem in the future and may require a lot of time, labor, and money to fix. It may be useful to use hand calculations to initialize the design process but not enough to solve complex problems on their own. The finite element analysis can be performed to determine initial design parameters. However, it requires a lot of time and considerable effort to solve the analysis as the complexity of the model increases. Moreover, structural tests might be beneficial to determine the conceptual design parameters. However, it can be very costly to test different types of structures in the early design stages. Unfortunately,

these time-consuming and expensive processes are carried out in the structural design stage of each various project. Therefore, an efficient method is required to overcome the difficulties of initializing the design. As a solution, artificial neural networks (ANNs) could be employed to develop a design tool for the fulfillment of this need since they are powerful models.

ANNs are self-learning computational models that can solve non-linear and complex problems using easy-to-understand algorithms. Neural network modeling is a sort of deep learning technique which has many applications, such as clustering, classification, and function approximation. Moreover, a neural network model needs a huge amount of data to be trained and develops its accuracy utilizing this training data. Once the network is well established with high precision, it becomes a robust tool to predict the desired outcome.

In this thesis, ANNs will be utilized to determine the static structural characteristics of the horizontal stabilizer of a helicopter. The database required to train the model to be developed will be provided by the finite element analyses. The analyses of the horizontal stabilizer will be performed under the aerodynamic pressure load for different design variables, the number of internal ribs, and the thicknesses of the structural components. These design variables will also be the inputs for the tool to determine the total displacement of the horizontal stabilizer and the maximum stresses occurring on the components of the stabilizer under the aerodynamic load.

In this study, it is aimed to develop a design tool to reduce the effort and time spent in the initial design phase of a helicopter. Furthermore, this study will be unique in combining the deep learning technique with structural engineering knowledge to determine the static structural characteristics of a helicopter component. Besides, the innovative approach presented in this thesis can trigger the creation of similar design tools for different components of aerospace structures.

The thesis consists of seven main chapters:

1. Introduction
2. Literature Review
3. Theoretical Background
4. Design and Analysis of the Horizontal Stabilizer
5. Artificial Neural Networks
6. Conclusion
7. References

After a brief introduction, Chapter 2 begins with the studies and research in the literature about artificial neural networks. Then, artificial neural networks and the design of experiments are explained extensively in Chapter 3. Afterward, the design and analysis process of the horizontal stabilizer of a helicopter is given, and the analysis results are discussed in Chapter 4. Chapter 5 exhibits the artificial neural network modelling procedure. Moreover, the performance of the design tool to be developed is presented with the results discussed. Concluding remarks and future works are shared in Chapter 6. Finally, the thesis ends with the references given in Chapter 7.

2. LITERATURE REVIEW

Applications of artificial neural networks (ANNs) have been growing intensely in the aerospace industry. ANN has become the method of choice in literature when it comes to making predictions about the concerning problems in the aerospace field [2]. Various applications of ANN exist in the literature, such as the prediction of stress, strain, and load. Many studies concerning ANN methodology make use of the finite element method (FEM), experiments, or a combination of them to make estimations since the self-learning ability of this methodology requires a considerable amount of data. Moreover, numerous applications can be created for use in aviation because ANN may become a robust computational model once it is well-established.

Extensive research has been conducted on the applications of artificial intelligence (AI) methods including neural networks (NNs) in structural engineering by Salehi & Burgueño [3]. The literature shows that AI applications in the structural engineering field have become more popular over the last decade due to the superior capabilities of these techniques.

Cooper et al. [4] have proposed an estimation technique using ANN to compute the static load applied on a wing rib. It was developed using the data generated from experiments and finite element analyses. In the beginning, a static test was conducted in which a wing rib was subjected to a range of compressive loads, and strain values were measured using the gauges attached to the structure. Following, the random data were generated using the strain values obtained from the test to be employed as training data. Moreover, the FEM of the wing rib was also created and calibrated based on the experimental test results to compose training data. ANN models trained using the strain values from the random data and the finite element analysis (FEA) results gave highly accurate load estimations. In the study of Jeong et al. [5], an ANN model has been designed to avoid redundant and expensive inspections after misjudged hard landing cases by predicting maximum loads and strains in certain structural regions. Similarly, Gómez-Escalonilla et al. [6] have exhibited a strain prediction method built within the advancement of the structural health monitoring system to be integrated into A330 aircraft. First, strain data were obtained

through the gauges attached to the main aircraft components of the aircraft with corresponding actual flight data. Using the data collected, neural network models were established for each component to estimate strains in the components. Surprisingly, the prediction results were highly encouraging with errors of less than 3.5%, although the training data had been generated using only 5% of the complete data.

A neural network-based design tool has been developed by Yıldırım et al. [7] for bolted flange connections subjected to axial loading. This tool calculates reaction force in the bolt and average von Mises stress in the flange using geometric and loading inputs such as the size and pretension of the bolts and structure thickness. In this study, it is concluded that the tool gives outstanding results within the training limits of the model; however, the accuracy of results reduces beyond the limits.

The stress concentration factor (SCF) of a reinforced hole in an infinite plate subjected to uniaxial and biaxial loading has been calculated through NNs in the study of Ozkan et al. [8]. Finite element results validated by experimental data were used to feed the network model. A significant advantage of this new approach is that the stress concentration factor is calculated by just specifying the geometrical and loading parameters to the model. Normally, an additional calculation is required to obtain SCF after obtaining the stress results from a simulation.

Ribeiro et al. [9] have evaluated the stress distribution over a plate with a hole under uniaxial tension load with the ANN approach. The model was built using the Python TensorFlow library. The database was generated using a finite element (FE) solver. RMSProp and Rectified Linear Unit (ReLU) were adopted as an optimizer and an activation function used in hidden layers of the network, respectively. A comparison of stress fields over a quarter of a plate obtained by the FE solver and ANN was also presented in this study as given in Figure 2.1. It was claimed that a significant time reduction in stress calculation was achieved using this approach. Ribeiro et al. [10] have conducted a similar study where the findings are promising. A plate and a reinforced panel were analyzed under uniform pressure. The ANN models were generated using the analysis results for different design variables. The displacement and von Mises stress

fields have been mapped over the structure. ReLU was used as an activation function, while RMSProp was preferred as an optimizer.
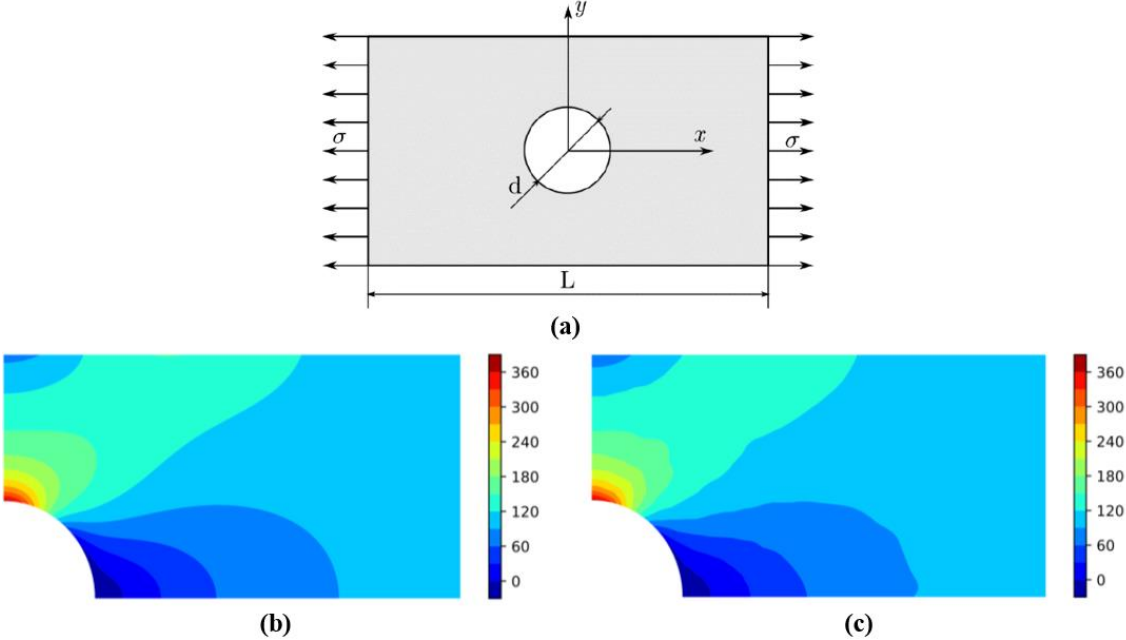
Figure 2.1 (a) Plate with a hole, (b) FEA Stress Result, (c) ANN Stress Prediction [9]

Rusia et al. [11] have created a stress analysis tool. Firstly, a triangular steel plate with a hole was analyzed under pressure loading. The analysis was diversified considering various pressure loadings applied and geometrical parameters which are the thickness and edge length of the plate and the hole diameter. Subsequently, the results of maximum deformation and maximum von Mises strain and stress were acquired for each analysis. These data were used in training the ANN. The predicted stress, strain, and deformation results for test samples have low absolute positive errors when considering FEM results. There are similar studies in the literature. Maximum elastic deformation of the raw material during machining has been determined for different fixture installation plans in the study of Selvakumar et al. [12]. Similarly, Ćojbašić et al. [13] have calculated the deformation of a thin-walled cylindrical shell structure using NNs for different load applications. Tosun et al. [14] have utilized NNs to predict the ultimate load of two bonded plates under tensile load shown in Figure 2.2. The training data feeding the model were obtained from experiments where the length and width of the bonded section were variables. Likewise, Sidda Reddy et al. [15] have proposed a technique combining NNs

6

and design of experiments (DOE) to determine the stress and deflection of the CFRP laminated panel under uniform load.
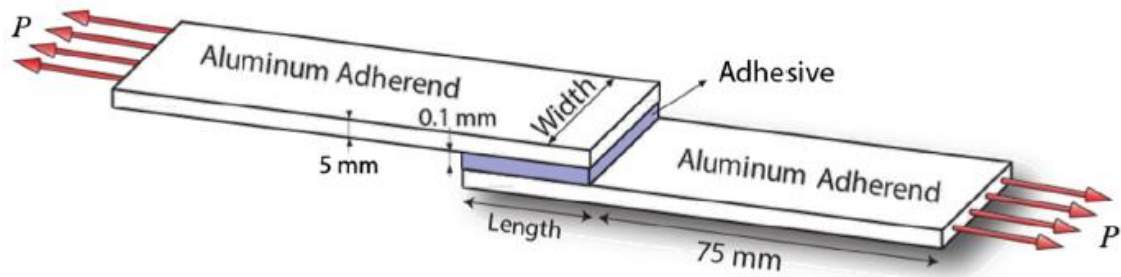
Figure 2.2 Bonded plates under tensile load [14]

Composite materials have substituted some conventional materials in aerospace structures due to their marvelous characteristics. However, their usage has some drawbacks, such that damage to composites can deteriorate their structural characteristics. Therefore, damage detection in composites is vital for flight safety. Regarding this matter, a variety of studies carried out about AI applications to identify the damage in composite materials have been presented by Das et al. [16]. Besides, it is hard to model the non-linear stress-strain behavior of composite materials. Mechanical tests are required; however, they are challenging to establish and can be very costly. Bezerra et al. [17] have made use of ANNs to model the shear stress-strain behavior of carbon/epoxy and glass/epoxy composites employing experimental tests. In the study of Zhang et al. [18], a comprehensive review of several applications of ANNs to predict particular mechanical properties of polymer composites has been compiled. Reddy et al. [19] have discussed ANN utilization to predict the natural frequency of composite laminate with the input of different ply angles. Moreover, Reddy et al. [20] have also examined the optimization of stacking sequence in composite laminates using DOE and NNs.

Buckling is the instability that causes the abrupt failure of a structural member [21]. Several studies have been carried out to overcome this problem by predicting the buckling load. In the study of Sun et al. [22], a neural network-based analysis tool has been established to predict the buckling and ultimate load of a hat-stiffened composite plate subjected to in-plane shear. The tool was established utilizing the analysis results of a

finite element model verified by an experimental test in advance. Similar buckling strength estimation tools have been developed for situations where a compressive load has been applied on a hat-stiffened composite plate by Kumar et al. [23] and a laminated composite panel with a central hole by Nicholas et al. [24]. Lastly, Guzel et al. [25] have computed buckling load prediction for integrally stiffened panels using ANN in combination with the Latin Hypercube Sampling (LHS) DOE methodology. LHS was used to decrease the number of FE analyses required for building a database feeding the network. Overall, NNs were found as remarkable computational models that can predict a structure's buckling behavior.

ANN is a preferred methodology in optimization problems as well. Paiva et al. [26] have compared surrogate models including ANN using aircraft wing design optimization problems to obtain a lower computational cost. It was recommended to use surrogate models in designing optimization problems to accelerate the optimization process. It was also stated that ANN may provide significant performance advantages as the problem becomes complicated.

ANN is not only employed in the design and analysis of structures but also in different disciplines of aerospace engineering. Yıldırım et al. [2] have used the ANN technique to predict the optimum thrust of an aircraft during take-off, cruise, and landing. The model was trained with real flight data from an Airbus A319 aircraft. It was concluded that the thrust of an aircraft could be estimated rapidly with a small relative error. In addition, various applications of ANN in the aerospace field were also described in this exclusive research. Secco et al. [27] have presented an ANN-based methodology to compute aerodynamic coefficients, namely, the lift and drag coefficients for different flow regimes. A similar study has been performed by Santos et al. [28]. The method based on the neural network model achieved convenient predictions of airfoil aerodynamic coefficients. It was explained that although the error for some coefficient predictions is not satisfactory, it can be reduced by using more neurons and training data.

3. THEORETICAL BACKGROUND

3.1. Artificial Neural Networks

Artificial neural networks (ANNs), also known as neural networks, are novel computational systems that emulate the biological nervous system network [28-29]. They are self-learning models that manage to solve complex problems using easy-to-understand algorithms. Unlike the conventional computational methods which use a complicated set of equations to address certain problems, ANNs solve problems by learning from experiences in the same way as the human brain. They can be implemented on a variety of problems due to their self-organizing ability. Neural network modelling is a kind of deep learning technique with numerous applications such as clustering, classification, and function approximation [30]. It is utilized in a wide range of industries including aerospace, automotive, electronics, and robotics.

A biological nervous system consists of billions of interconnected neurons. Each neuron functions as an information processor. The parallel processing capability of neurons and their interactions bring different abilities to the brain. These neurons are composed of dendrites, soma, axon, and synapse as shown in Figure 3.1. Dendrites collect the incoming signal or data and carry the signal to the soma. Then, the soma, which is the cell body, processes the data using its nucleus. The generated data is transmitted to other neurons at synaptic terminals through a tubular fiber called the axon. The connection between neurons is made through synapses.
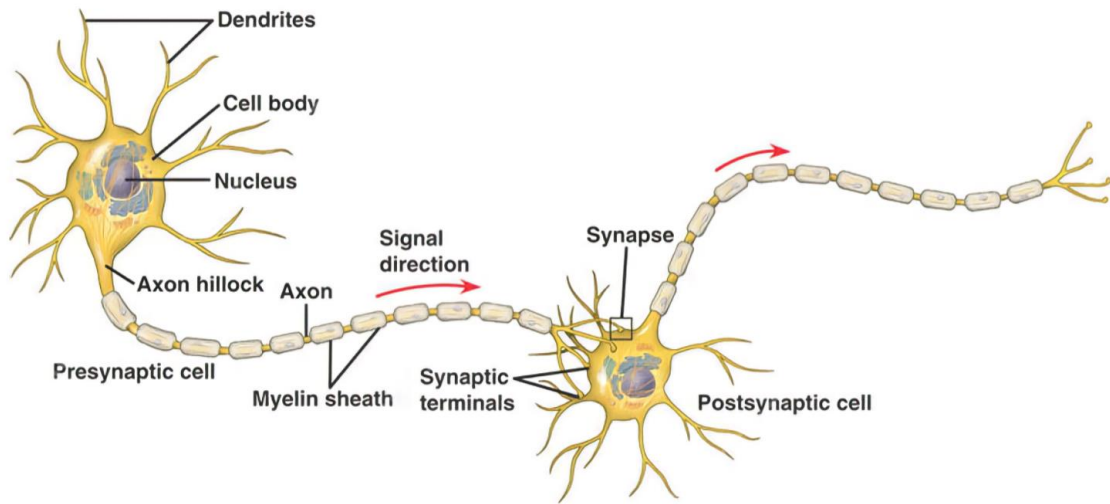
Figure 3.1 Biological Nervous System Cells [31]

Analogous to the biological neural network, an ANN is composed of numerous artificial neurons which are connected to each other layer by layer. An artificial neuron, also known as a perceptron, is the essential data-processing unit of a neural network [32]. The common structure of an artificial neuron is depicted in Figure 3.2.
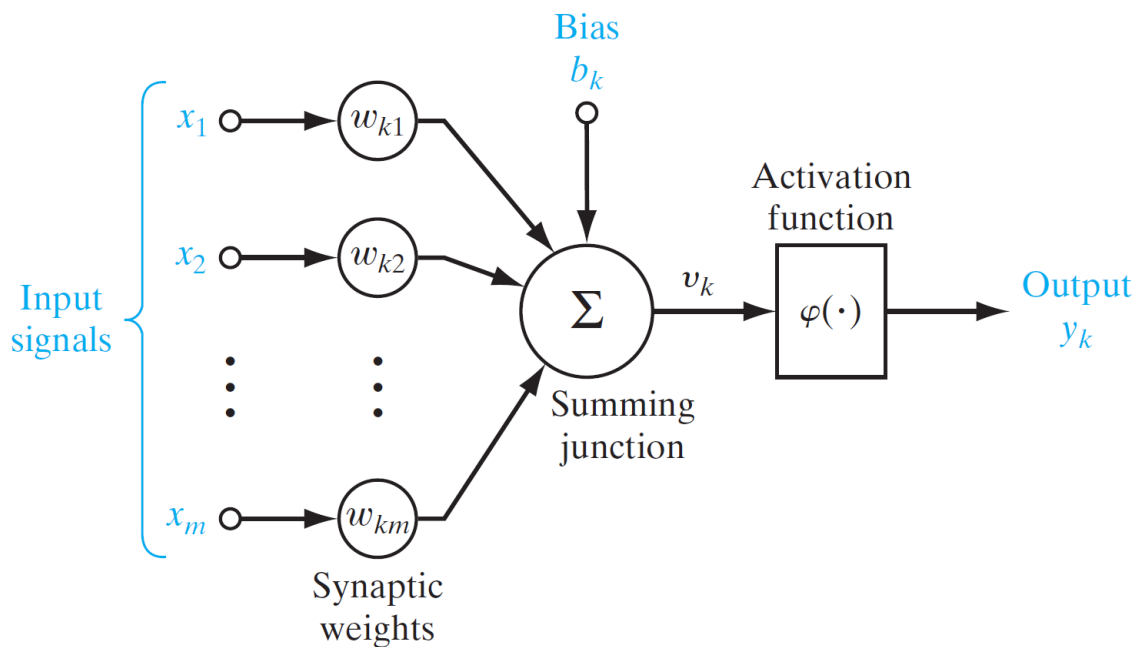
Figure 3.2 Common Structure of an Artificial Neuron [32]

As shown in Figure 3.2, input signals or data coming from neighboring neurons are received through connections or dendrites. Each connection has a specific weight. Some inputs have a greater impact than others on the unit which generates a neural response. So, synaptic weights act as adjustable coefficients to assess how important the incoming input signal is to the output [33]. When the inputs flow through the connections, the neuron computes the weighted sum of the signals by adding a constant called bias as given by Equation (3.1). Bias is an extra parameter that brings flexibility to the neural network.

$$v_k = \sum_{i=1}^{m} w_{kj} x_j + b_k \qquad (3.1)$$

The obtained value becomes only the linear combination of weights and inputs with a bias. Moreover, performing complex tasks using such a linear model would not be possible. Therefore, the output is further processed using an activation function as shown by Equation (3.2).

$$y_k = \varphi(v_k) \qquad (3.2)$$

The learning process of an ANN is achieved by adjusting the weight and bias parameters. The output processed gets closer to the target value as a result of tuning these parameters by the learning process. The effect of weight and bias in neural networks can be visualized using a sigmoid activation function employed in neural network applications. As seen in Figure 3.3, the sigmoid function only varies with the weight parameter. In addition, Figure 3.4 illustrates how the function changes with the change of bias while the weight parameter is kept constant.

As can be understood from Figure 3.3, the graph gets steeper as the weight increases. Otherwise, it becomes smoother. Therefore, the weight parameter changes the shape of the graph.
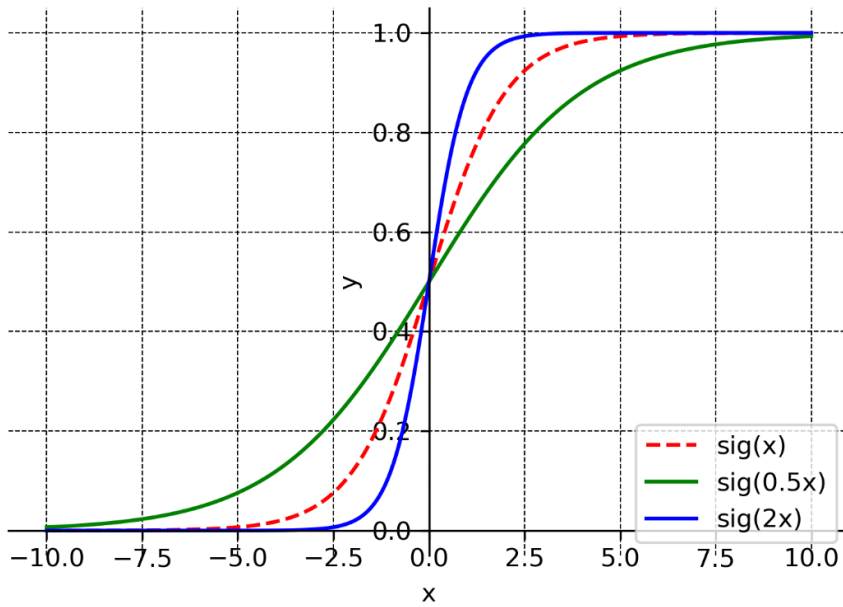
Figure 3.3 Effect of Weight Change in Neural Networks

Bias simply shifts the activation function graph as seen in Figure 3.4. It does not change the shape of the curve. Using a bias parameter additional to the weight parameter provides better generalization capability in this manner.
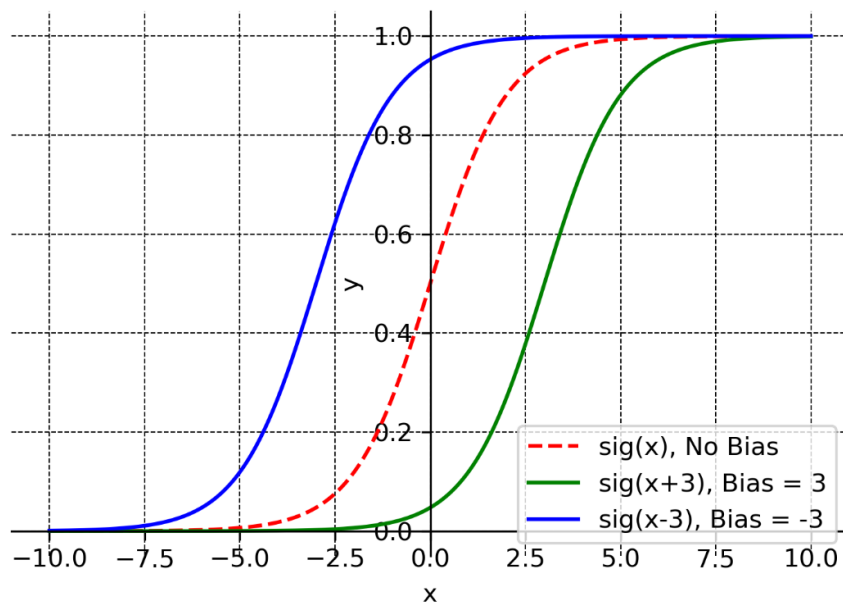
Figure 3.4 Effect of Bias Change in Neural Networks

As it can be concluded, the weight and bias parameters are crucial for the learning procedure of NNs. However, without activation functions, ANNs would not be powerful models.

An activation function introduces non-linearity to the network and allows the network to carry out challenging tasks. Furthermore, it determines whether the neuron gets activated or not, i.e., if the incoming data will be delivered to the neighboring neuron [34]. There are many activation functions developed for NNs. The sigmoid function, the hyperbolic tangent function, and the rectified linear unit (ReLU) function are popular activation functions in NNs.

The sigmoid function converts any real values to values in the range of 0 to 1. It is mathematically defined as in Equation (3.3).

$$sig(x) = \frac{1}{1 + e^{-x}} \qquad (3.3)$$

The sigmoid function is depicted in Figure 3.5. The function clearly levels out beyond the -3 and +3 regions. The gradient of the function turns into a pretty small value in these sections. This leads to a vanishing gradient problem which fundamentally causes a slowdown in the learning process of the NNs.
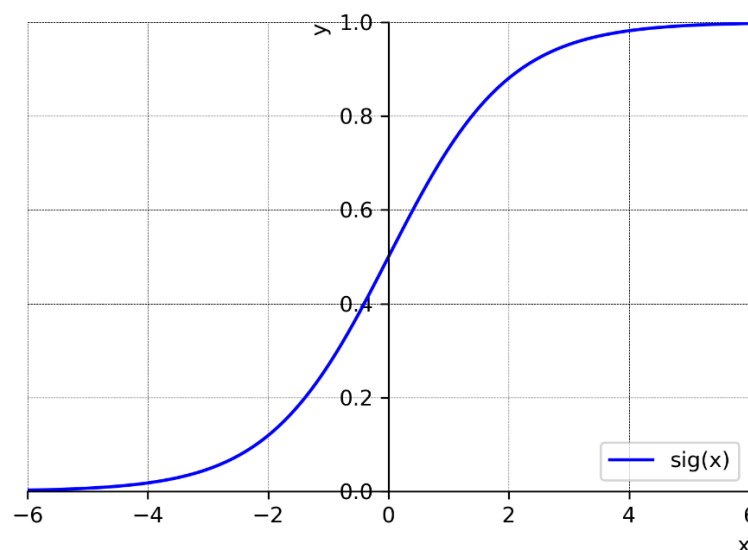
Figure 3.5 The Sigmoid Function

The hyperbolic tangent function resembles the sigmoid function. It provides an output within the range of -1 to 1. It is formulated as in Equation (3.4).

$$\tanh(x) = \frac{\sinh(x)}{\cosh(x)} = \frac{e^x - e^{-x}}{e^x + e^{-x}} \qquad (3.4)$$

The hyperbolic tangent function is indicated in Figure 3.6. Although the network model with the hyperbolic tangent function is quicker than the model with the sigmoid function, it is as vulnerable as the sigmoid function to the issue of vanishing gradients.
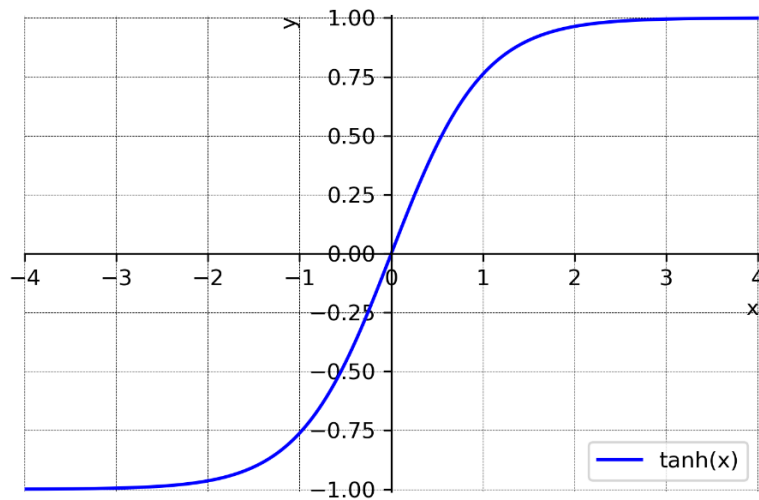
Figure 3.6 The Hyperbolic Tangent Function

One of the most widely used activation functions is the rectified linear unit (ReLU) function whose output lies between 0 and infinity. It outperforms the sigmoid and hyperbolic tangent activation functions in terms of computational efficiency since only a portion of neurons is activated at once rather than all [35]. Moreover, it overcomes the vanishing gradient problem that other activation functions suffer from. Hence, the use of ReLU has become the default suggestion in contemporary NNs [36]. It is mathematically represented in Equation (3.5).

$$\text{ReLU}(x) = max(0, x) = \begin{cases} x \ if \ x \geq 0 \\ 0 \ if \ x \ < 0 \end{cases} \qquad (3.5)$$

The ReLU activation function is also illustrated in Figure 3.7.
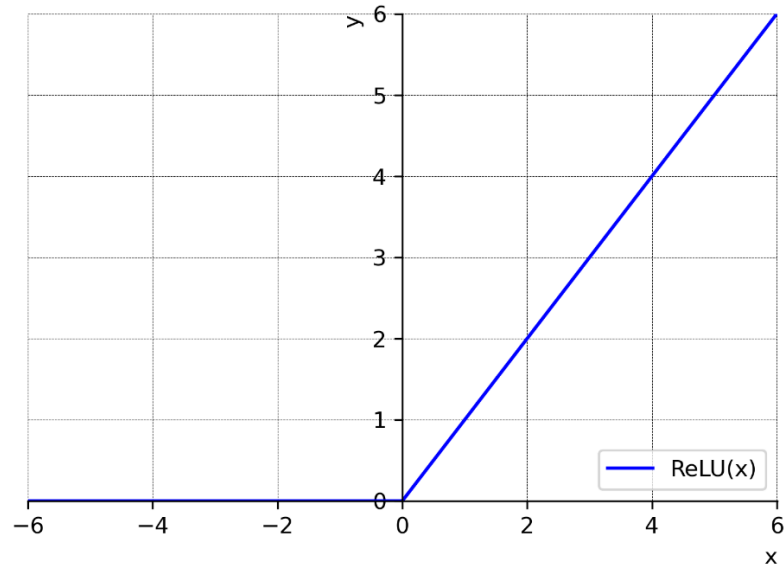
Figure 3.7 The Rectified Linear Unit Function

Artificial neurons or perceptrons constitute ANNs. One of the primary and multi-functional network architectures is the multilayer perceptron (MLP) where the input data flows forward through fully connected layers of artificial neurons. An MLP includes three primary layers: the input layer, the output layer, and the hidden layers located between them as shown in Figure 3.8.
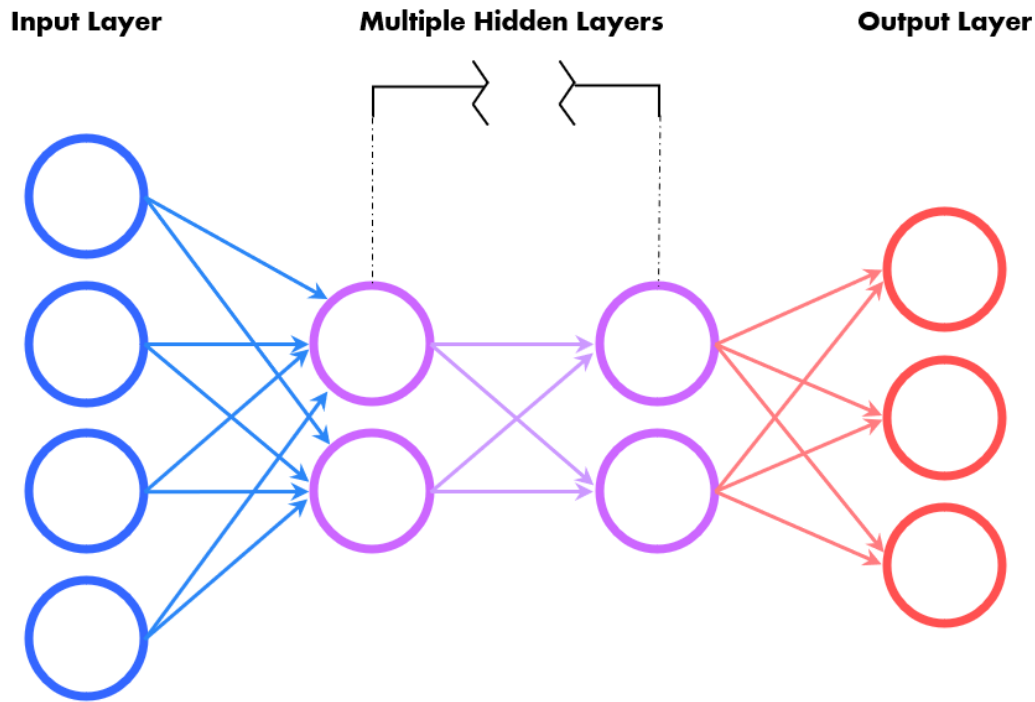
Figure 3.8 The Structure of an ANN

As the name suggests, the input layer feeds the input data into the model without any calculations made. The number of neurons in the input layer obviously equals the number of input variables. Hidden layers then process the information delivered by the input layer and transmit it to the output layer. The output layer is the last layer where the ultimate results are obtained. The number of neurons in the output layer is equal to the number of targets. When there are multiple targets, a multi-output network model can be created as well as a single-output multi-network model [37].

Neural network models can consist of many hidden layers. Nonetheless, a single hidden layer is adequate for the majority of fitting problems [37]. The necessary number of hidden layers and neurons in each are determined considering the problem and its complexity as well as depending on the data feeding into the model [30]. They have a critical impact on the performance of the model. However, there is no certain method to determine them. Therefore, the trial-and-error approach is usually preferred to decide on these network configuration parameters. If the number of neurons in hidden layers is insufficient, the network may not perform well. Increasing the neuron's quantity in the hidden layers is sometimes necessary to enhance the model's performance. For example,

let us consider a network model with a hidden layer of two to five neurons. As shown in Figure 3.9, as the number of neurons in the hidden layer is increased, the network model better approximates the actual model.
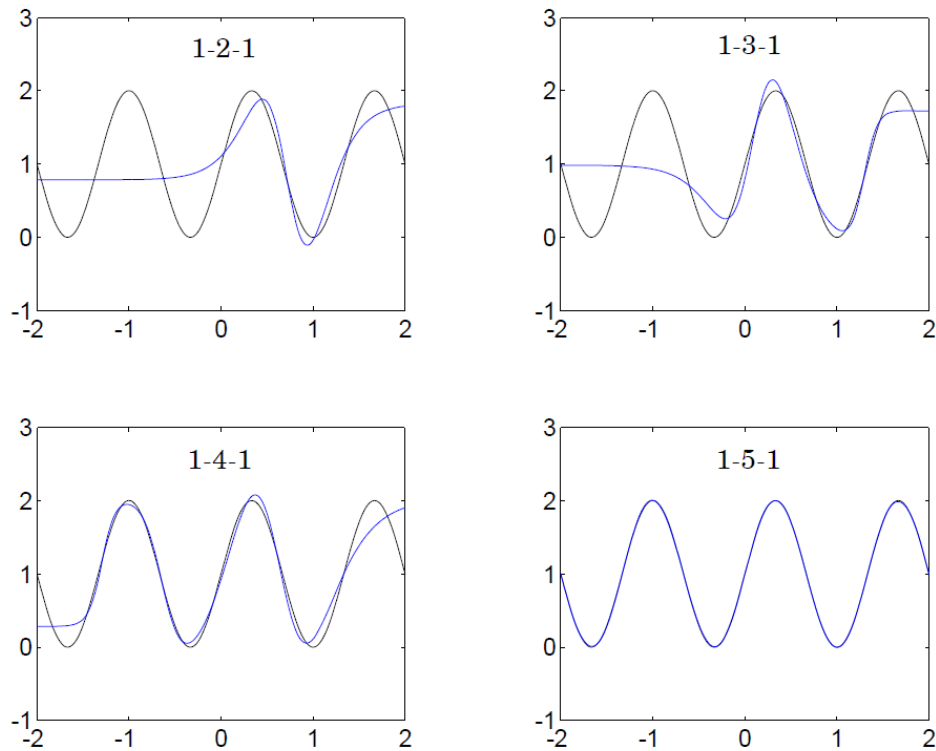
Figure 3.9 An Example of Increasing the Number of Neurons in Hidden Layers [37]

On the other hand, a rise in the number of perceptrons in hidden layers causes the network model to become more complicated. Using more neurons than necessary in hidden layers leads to another problem which is called the overfitting problem. This problem occurs when the network model memorizes the training data and becomes unable to generalize from the input-output relationship [18]. Using too much training data also causes this problem [32]. Figure 3.10 shows the comparison between an adequately fitted model and an overfitted model.
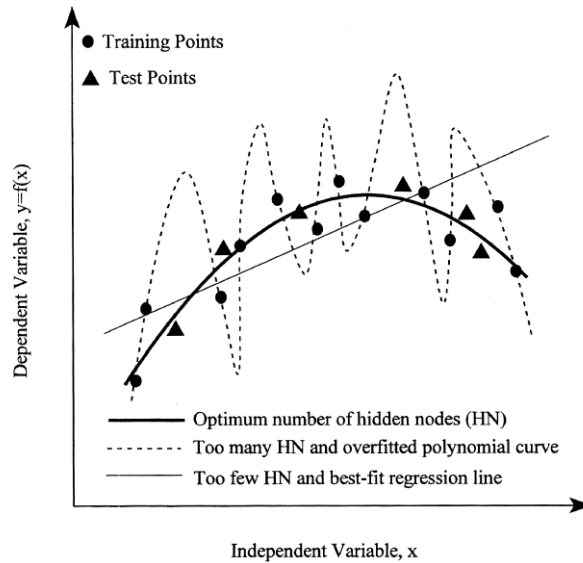
Figure 3.10 Overfitting Problem [34]

As seen in Figure 3.8, the input data progresses across the network in the forward direction layer by layer up to the output layer. This process is called forward propagation. Once the output is acquired after the input propagates to the output layer, an error will occur owing to the difference between the prediction and the target. This error is measured by a cost function. It is then propagated back into the network to minimize the error by adjusting weights and biases using the backpropagation training algorithm. Thus, the minimization of the cost function produces more accurate results [38]. This process is represented in Figure 3.11.
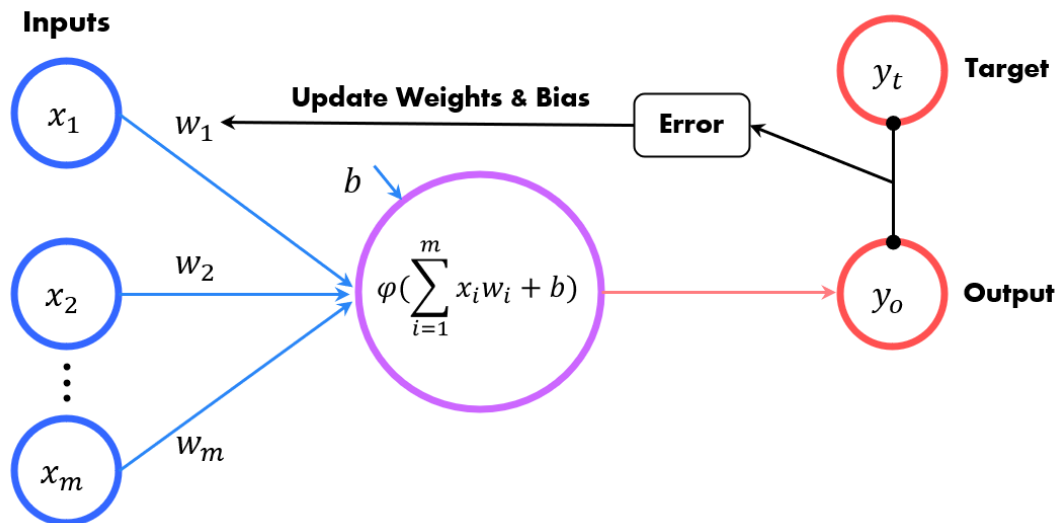
Figure 3.11 Forward and Back Propagation Cycle

Mean squared error (MSE) is commonly used as a cost function to measure the error [39]. It is given in Equation (3.6).

$$\text{MSE} = \frac{1}{N} \sum_{1}^{N} (y_t - y_o)^2 \qquad (3.6)$$

where y_t is the actual or target value, y_o is the output value and N is the number of samples.

As mentioned before, during the training of an ANN model, the optimum value of the weights and biases is determined through an optimization algorithm. The main purpose of the optimization algorithm, also called the learning algorithm, is to calibrate the network in order to get close estimates to the target values [30]. The gradient descent algorithm is the common choice to optimize NNs [40]. It is an iterative method to minimize the cost function by changing the parameters at each iteration in the opposite direction of the function's slope as shown in Figure 3.12. There are also second-order optimization algorithms such as Newton's method and Levenberg Marquardt. However, they become inefficient for higher dimensional problems [39-40].
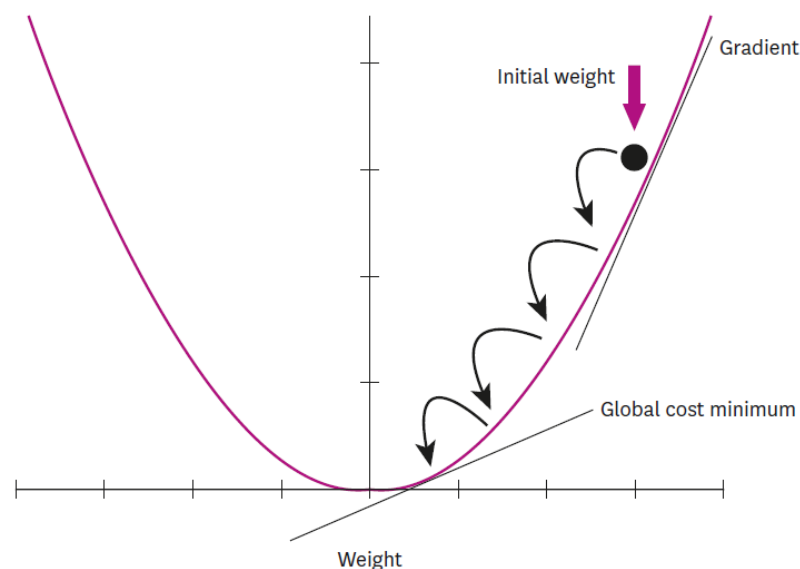
Figure 3.12 Minimization of a Cost Function with the Gradient Descent [38]

The commonly used gradient-based optimization algorithms are stochastic gradient descent (SGD) with momentum, root mean square propagation (RMSprop), and adaptive moment estimation (Adam) [36]. Adam optimizer is the combination of momentum and RMSprop algorithms. It is a highly efficient stochastic optimization algorithm requiring less memory and is suitable for non-convex problems containing large numbers of data or parameters [42]. It utilizes first-order gradients which makes Adam simple to implement. The algorithm is as follows:

Adam Optimization Algorithm

Inputs:
α: the learning rate

β_1 and β_2 : the exponential decay rate parameters

Initialize:
$m_0 = 0$

$v_0 = 0$

Loop: Continue until convergence

Calculate the gradient of the objective function, $f(\theta)$:

$$g_t = \nabla_\theta f_t(\theta_{t-1})$$

Update exponentially weighted averages, m_t and v_t:

$$m_t = \beta_1 . m_{t-1} + (1 - \beta_1) . g_t$$

$$v_t = \beta_2 . v_{t-1} + (1 - \beta_2) . g_t^2$$

Calculate the bias-correction:

$$\widehat{m_t} = \frac{m_t}{1 - \beta_1^t}$$

$$\widehat{v_t} = \frac{v_t}{1 - \beta_2^t}$$

Update θ (i.e., weights or biases):

$$\theta_t = \theta_{t-1} - \alpha . \frac{\widehat{m_t}}{\sqrt{\widehat{v_t}} + \epsilon}$$

End Loop

The algorithm consists of an objective function or cost function, $f(\theta)$ to be minimized using weights or biases denoted by θ. First, the gradient with respect to θ is computed. Then, the exponentially weighted average of the gradient and exponentially weighted average of the squared gradient are calculated by initializing m_0 and v_0 to zero. The reason why they are called exponentially weighted averages is that they include the exponential average of recent gradients. Moreover, m_t is initially derived for SGD with momentum optimization algorithm, whereas v_t is formulated for the RMSprop optimization algorithm. In the algorithm, β_1 and β_2 manage the decay rates of these averages. The correction terms, $\widehat{m_t}$ and $\widehat{v_t}$ are introduced in the algorithm to keep the averages unbiased initially. Finally, θ at time t, (i.e., weights and biases) is updated. The algorithm iterates until convergence is achieved.

3.2. Design of Experiments

Design of experiments (DOE) is a method for selecting a group of samples from the design space to maximize the information extraction from a finite number of samples [43]. It is a way of efficiently performing different experiments on design concepts and a highly beneficial technique for organizing experiments and examining the outcomes. It enables minimizing the number of experiments required to obtain the necessary information. There are many types of DOE. The widely used types are as follows:

- Full factorial design
- Monte Carlo sampling
- Latin hypercube sampling
- Hammersley sampling

Full factorial design is one of the classical DOE techniques. It considers all possible combinations of design variables. Let us suppose a design consisting of *m* design variables with *n* levels. In this case, a full factorial design creates n^m number of experiments. This method can be useful in analyzing a small number of experiments. However, it becomes costly as the number of variables and their levels increases.

Monte Carlo, Latin hypercube, and Hammersley sampling are common modern DOE methods. Monte Carlo sampling is a method that relies on pseudorandom number generation for a uniform distribution approximation [44]. That is the reason it is also called pseudo-Monte Carlo sampling. Although it is straightforward to use, significant portions of the design space remain uncovered with the group of Monte Carlo samples used due to the nature of randomness.

Latin hypercube sampling is one of the prominent modern DOE techniques, which is derived initially as an alternative to pseudo-Monte Carlo sampling [43]. The range of each design variable is partitioned into k intervals with the same probability for k samples. Therefore, for l design variables, this division results in k^l intervals in the design space. Then, k samples are arbitrarily chosen in the design space considering two main rules. They are randomly positioned within an interval, and only one sample can be placed in each interval for each one-dimensional projection of the samples. This stratification technique's fundamental drawback is its poor uniformity characteristics on a unit hypercube [44].

Hammersley sampling is another modern DOE method. It is based on a deterministic mathematical formula producing a uniformly distributed sample pattern with a stochastic appearance [45]. It achieves notable computational savings with higher accuracy [44]. Moreover, it has better uniformity properties than Monte Carlo and Latin hypercube sampling since it provides an optimal design to place the samples.

Figure 3.13 compares Monte Carlo, Latin hypercube, and Hammersley DOE techniques for 100 samples. Among these three methods, Hammersley sampling acquires the most uniform distribution. Other methods have clustered patterns with unexplored space.
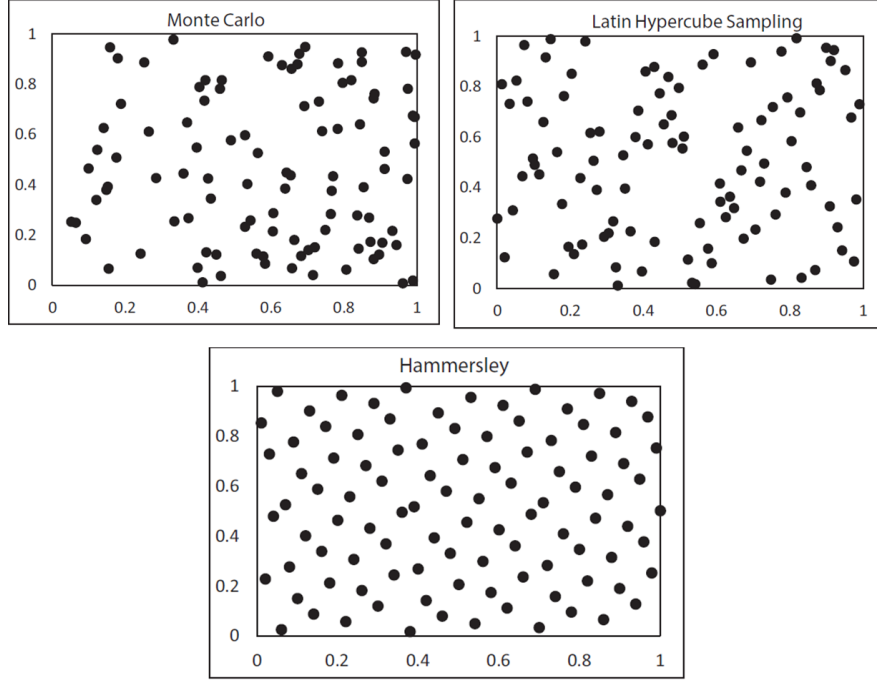
Figure 3.13 100 Samples with Different Methodologies [46]

The Hammersley sampling methodology can be explained mathematically as follows. Any positive integer (i) can be represented by a prime base (b) through Equation (3.7) where a_j is an integer coefficient in [0, b-1].

$$i = \sum_{j=0}^{r} a_j b^j = a_0 + a_1 b + a_2 b^2 + \cdots + a_r b^r \qquad (3.7)$$

Then, a function $\phi_b(i)$ can be constructed using Equation (3.8).

$$\phi_b(i) = \sum_{j=0}^{r} \frac{a_j}{b^{j+1}} = \frac{a_0}{b} + \frac{a_1}{b^2} + \frac{a_2}{b^3} + \cdots + \frac{a_r}{b^{r+1}} \qquad (3.8)$$

Finally, the Hammersley points in d-dimensional space can be determined using Equation (3.9) for $i = 0, 1, 2, \ldots, N$-1 where N is the total number of points.

$$x_i = \left(\frac{i}{N}, \phi_{b_1}(i), \phi_{b_2}(i), \ldots, \phi_{b_{d-1}}(i) \right) \qquad (3.9)$$

4. DESIGN AND ANALYSIS OF THE HORIZONTAL STABILIZER

This thesis aims at determining the static structural characteristics of the horizontal stabilizer of a helicopter with the ANN-based design tool to be developed. The ANN model needs a high amount of data for the training phase. This training data can be provided by performing finite element analysis (FEA) as well as conducting structural tests. Using the results of FEA will be sufficient to present the methodology within this research. For this reason, the geometry of the horizontal stabilizer will be determined first. Then, the finite element model of the stabilizer will be created after the calculation of the aerodynamic loads exerted on it. Finally, the required training data for the ANN model will be created by performing several parametric analyses.

4.1. Description of the Horizontal Stabilizer

A horizontal stabilizer is a wing mounted in the tail region of a helicopter. It essentially stabilizes the pitch movement of the helicopter. Basically, the helicopter tends to pitch the nose down in forward flight due to the total rotor thrust (TRT) of the main rotor. So, the downward aerodynamic force on the horizontal stabilizer increases. Thus, the horizontal tail lifts the nose by opposing the pitch behavior of the rotor, and it contributes to the longitudinal stability of the helicopter as shown in Figure 4.1.
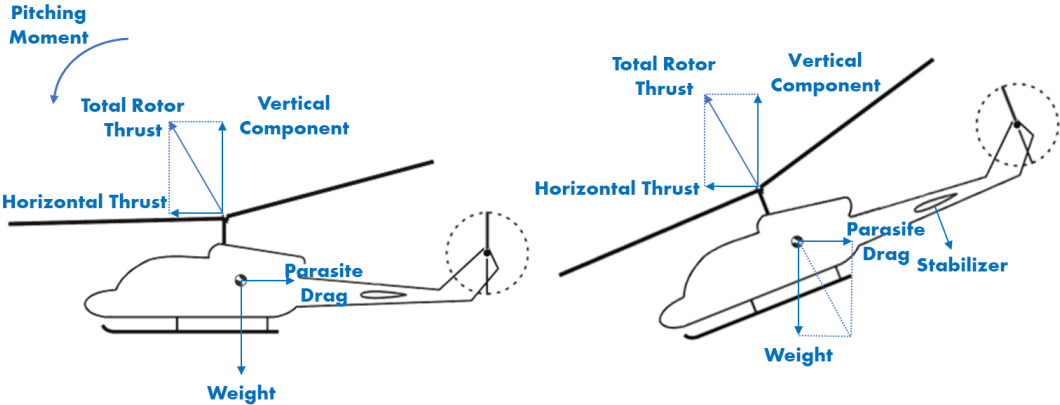
Figure 4.1 A Helicopter in Forward Flight (adapted from [47])

The horizontal stabilizer is a wing composed of three main structural elements, namely, skin, ribs, and spars, as indicated in Figure 4.2. The skin surrounds the inner structure and creates an aerodynamic force. It withstands normal and shear stresses. Ribs are the members placed along the chordwise direction. They preserve the airfoil shape by assisting the skin. Spars are the principal load-carrying members located along the spanwise direction inside the wing. They carry bending and shear stresses as well as stabilize the skin.
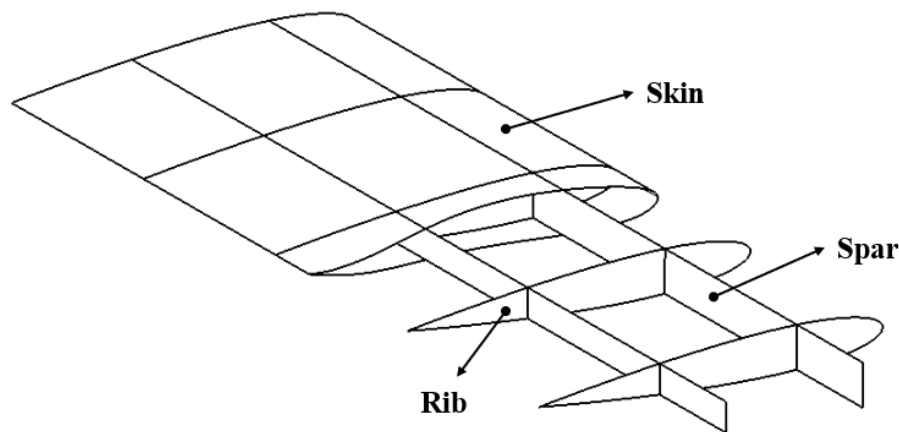
Figure 4.2 Structural Elements of a Horizontal Stabilizer

4.2. The Geometry of the Horizontal Stabilizer

In this thesis, the stabilizer dimensions are determined according to the approximate dimensions of the AW139 helicopter's stabilizer. Accordingly, the horizontal stabilizer will have a wingspan of 3500 mm and a chord length of 655 mm. Normally, they are decided considering different aspects of engineering disciplines such as performance, flight mechanics, aerodynamics, and structural design and analysis. In addition, the details of the AW139 helicopter are not accessible due to the project's classification. Therefore, the airfoil profile and the angle of attack of the horizontal stabilizer are designated considering the literature [48]. So, the stabilizer will have a NACA0012, symmetric airfoil profile with an angle of attack of -3°. Although the airfoil is symmetric, the wing will produce a downward aerodynamic force in forward flight because it has a negative angle of attack.

Spars are critical load-carrying members of a wing as mentioned before. The front spar is usually located between 15 and 30% of the chord, while the typical location of the rear spar is between 65 and 75% of the chord [49]. The rear spar is located at 65% of the chord to leave adequate space for the remaining fraction of the ribs behind the spar. To position the front spar, it is necessary to find out the center of pressure and the aerodynamic center as well. The center of pressure is the point where the resultant aerodynamic force acts upon a body, whereas the aerodynamic center is the location on an airfoil where the aerodynamic moment does not vary with the angle of attack. Theoretically, the quarter-chord point is the center of pressure and the aerodynamic center for a symmetric airfoil [50]. Therefore, it is wise to locate the front spar at 25% of the chord.

Horizontal stabilizers are created for three different rib configurations so that the ANN-based design tool developed in this thesis can use the number of internal ribs as an input. These are two, three, and four internal ribs. Moreover, they are modelled using surface elements to reduce the computation time of the structural analysis in generating an ANN input database. Only the left portion of the horizontal stabilizer will be considered in this study due to symmetry as shown in Figure 4.3.
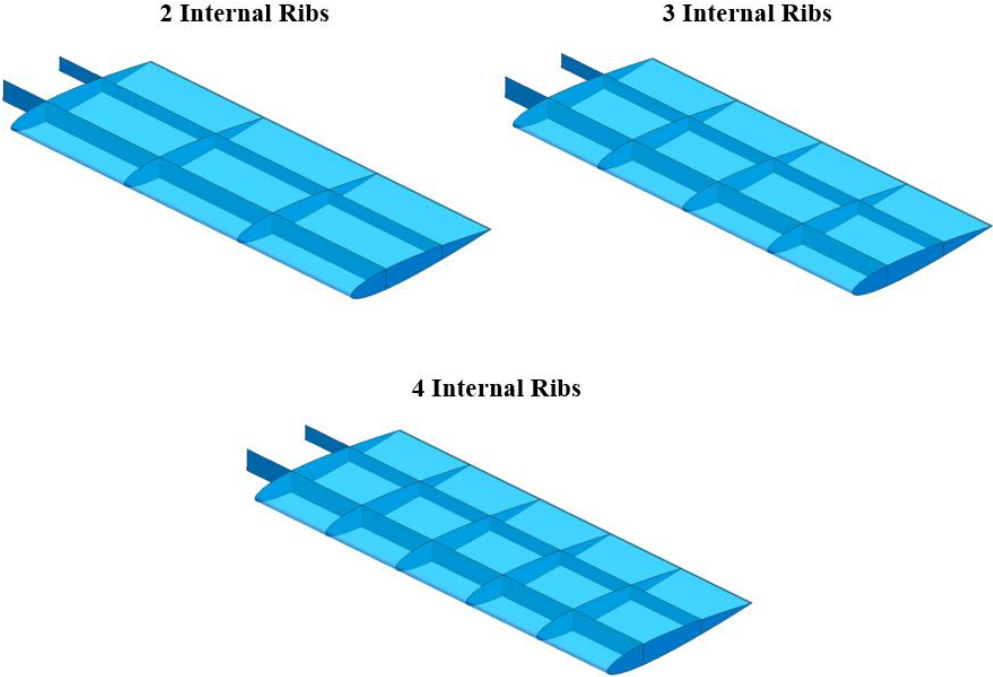
Figure 4.3 Wing Designs for Different Rib Configurations

Although there are three configurations of the wing, the outer geometry of the wing does not change. Therefore, the aerodynamic load for these wings will be the same for the same flight condition.

In the following section, an aerodynamic analysis will be performed to calculate the pressure load acting on the wing.

4.3. Calculation of the Aerodynamic Load

Before the structural analysis of the wing is performed, the aerodynamic load on the wing is determined by running a CFD analysis. The design of the wing is shaped according to the load to which the wing is subjected. Multiple load cases can be created to size the structure of the wing. These load cases are determined considering various aspects of the helicopter design. However, stabilizers are typically configured to work best at the forward cruise flight [51]. Consequently, it is considered that the cruise flight condition is sufficient to describe the ANN methodology developed in this thesis.

The maximum cruise speed of the AW139 helicopter whose horizontal stabilizer is to be analyzed is 165 knots (84.88 m/s). The stabilizer has a NACA0012 symmetric airfoil profile with an angle of attack of -3° as mentioned earlier. As a CFD analysis tool, ANSYS Fluent is used to calculate the pressure distribution over the wing [52]. An air box is created around the wing as a 3D computational domain which is indicated in Figure 4.4. The pressure far-field boundary condition is used when the flow is very far away from the disturbance source and becomes uniform [53]. It is situated about 20 body lengths from the wing [54]. So, the far-field is identified to the boundary of the domain which is shown by dark blue color. The symmetry boundary condition is used on the boundary indicated by the pink color as the half span is used in the analysis. Finally, the wall boundary condition is applied to the yellow region which is created to simulate the flow through the fuselage towards the wing and the flow over the wing.
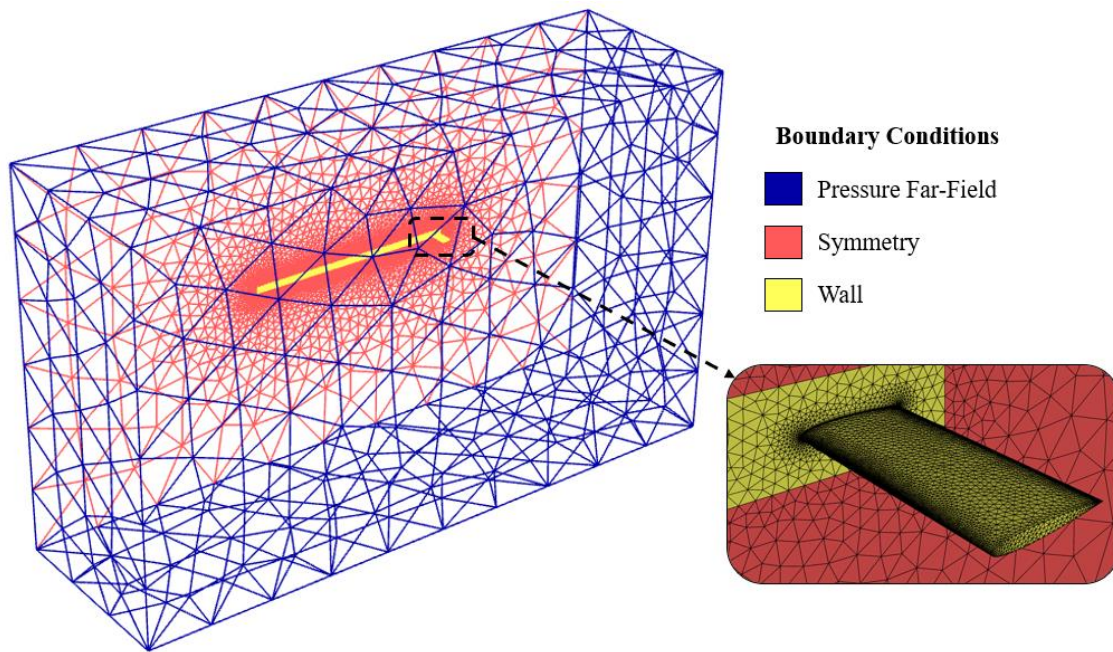
Figure 4.4 Boundary Conditions used in the CFD Analysis

The inside of the computational domain seems empty in Figure 4.4; however, it is actually full of meshes. The mesh around the wing is depicted in Figure 4.5. It is clearly seen that the grid is employed near the wing surface to include the effect of the boundary layer development along the surface as well as the potential flow separations in the model.
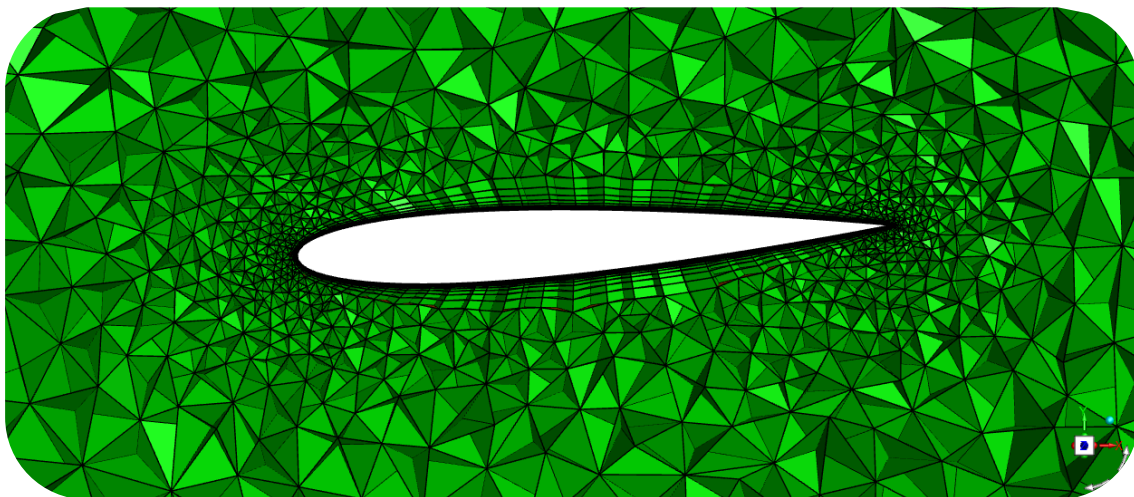
Figure 4.5 Mesh around the Wing

As the results of the analysis, the static pressure distribution over the wing is obtained as shown in Figure 4.6 and Figure 4.7. It is seen that the pressure distribution on the upper skin is higher than on the lower skin which results in negative lift generation, as expected.
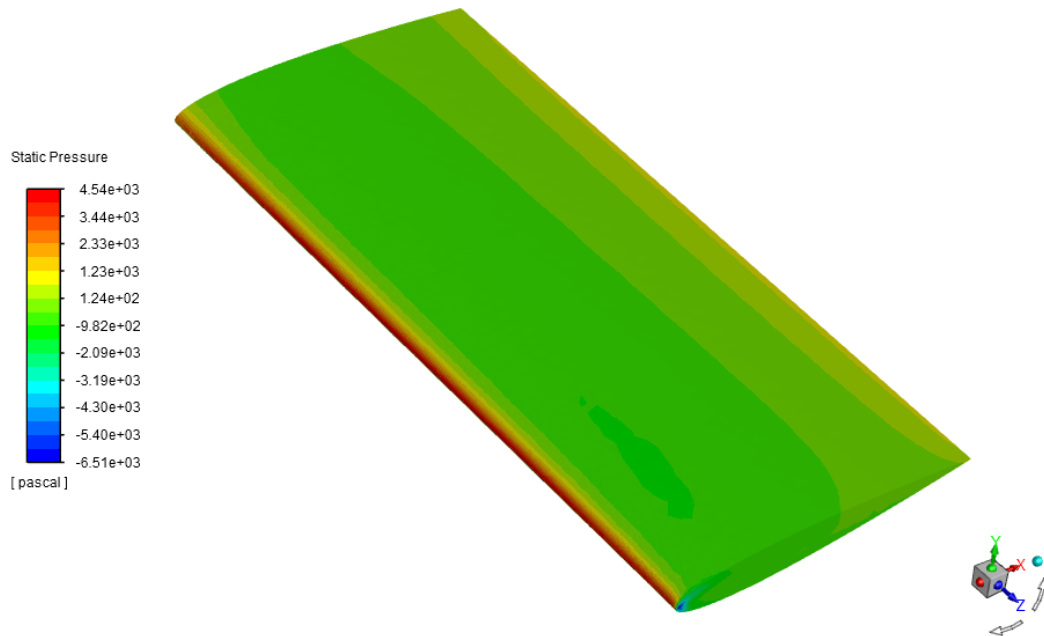
Figure 4.6 Static Pressure Distribution from the Top View
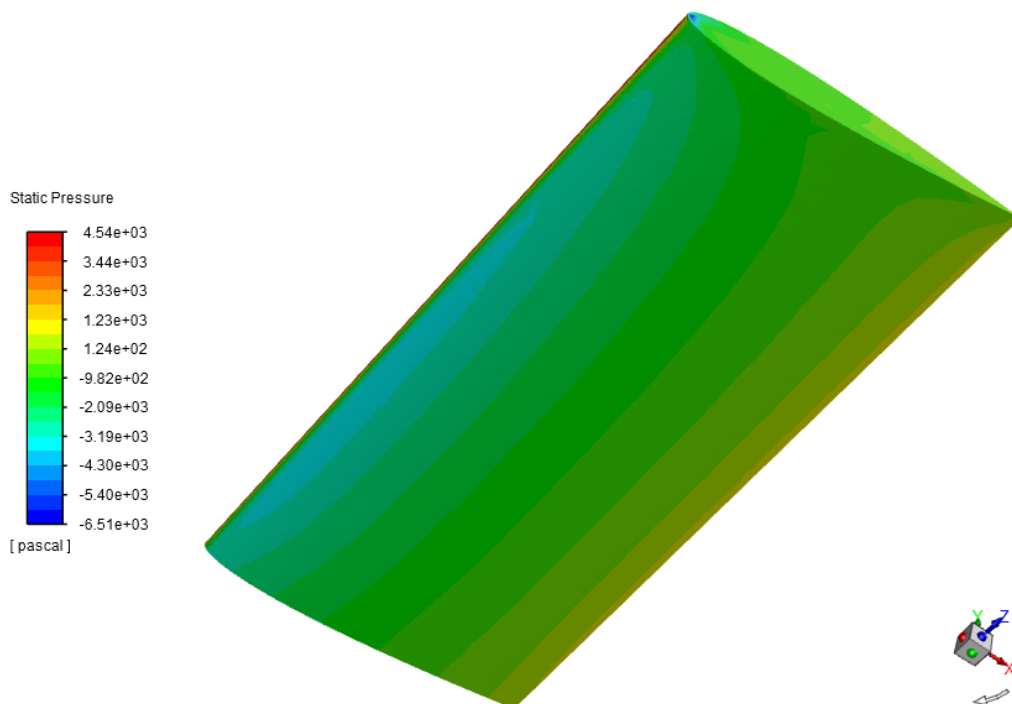
Figure 4.7 Static Pressure Distribution from the Bottom View

The streamlines across the wing are indicated in Figure 4.8. The air flows at 165 knots (84.88 m/s) towards the wing and then accelerates around the wing. Since the pressure on the upper skin is much higher than on the lower skin, the airflow around the wing tip tends to move downward and create vortices.
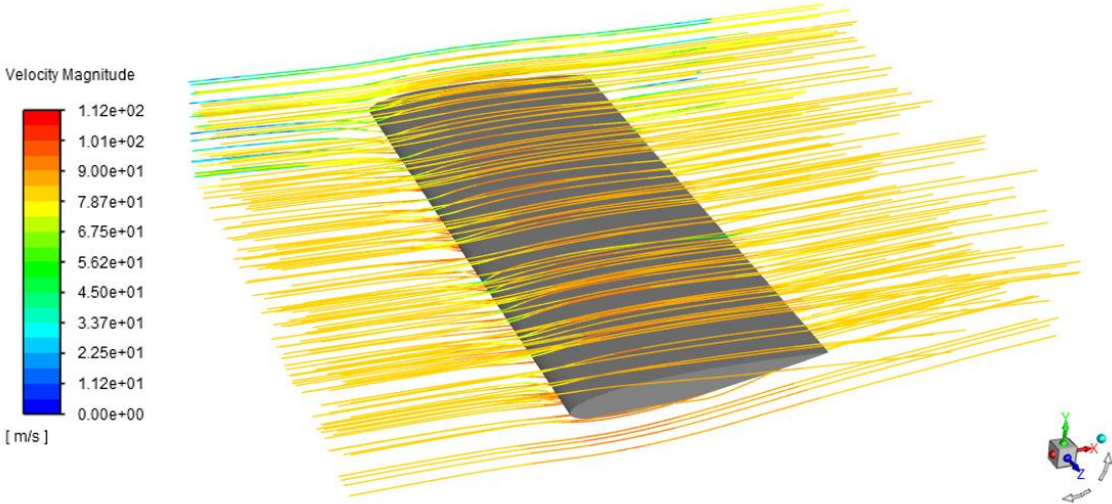
Figure 4.8 Streamlines across the Wing

Lastly, the resulting pressure data shown in Figure 4.6 and Figure 4.7 is interpolated onto the structural mesh to be used as a load boundary condition in the structural analysis using Tecplot 360 [55]. In this context, the inverse distance interpolation method is used. However, since the structural analysis and CFD analysis are based on distinct approaches, the type and size of the mesh applied on the wing in these analyses differ from each other. The interpolation accuracy rises as the structural mesh density increases. However, as the structural mesh gets finer, the computational effort becomes costly. Therefore, it would be wise to adjust the balance between them.

In Figure 4.9 and Figure 4.10, the actual pressure distribution on the upper skin is compared with the interpolated pressure distribution for fine structural mesh.
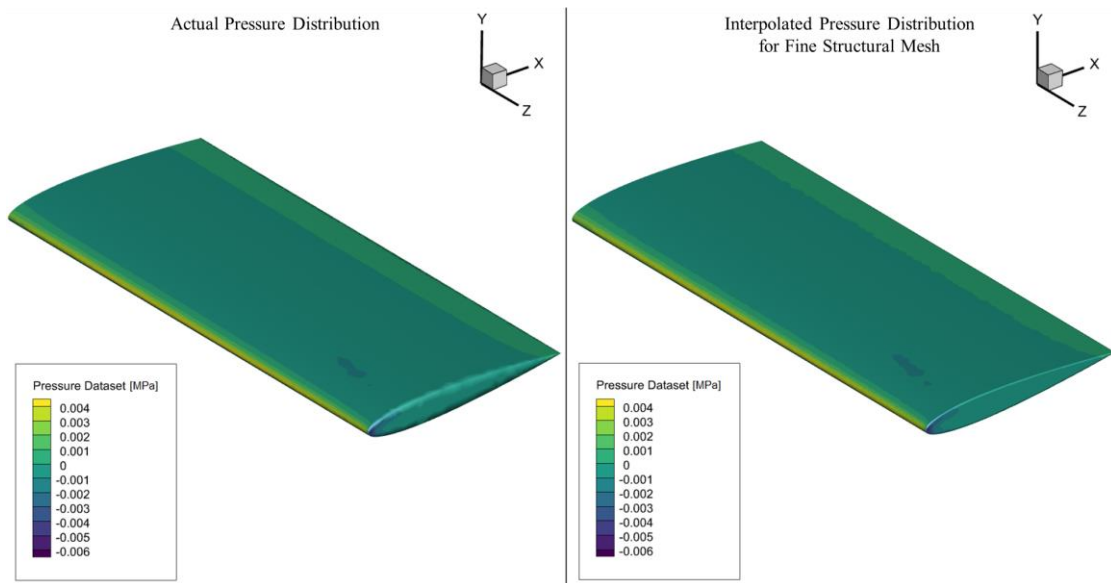
Figure 4.9 Comparison of Actual Pressure with Interpolated Pressure for Fine FE Mesh on the Upper Skin
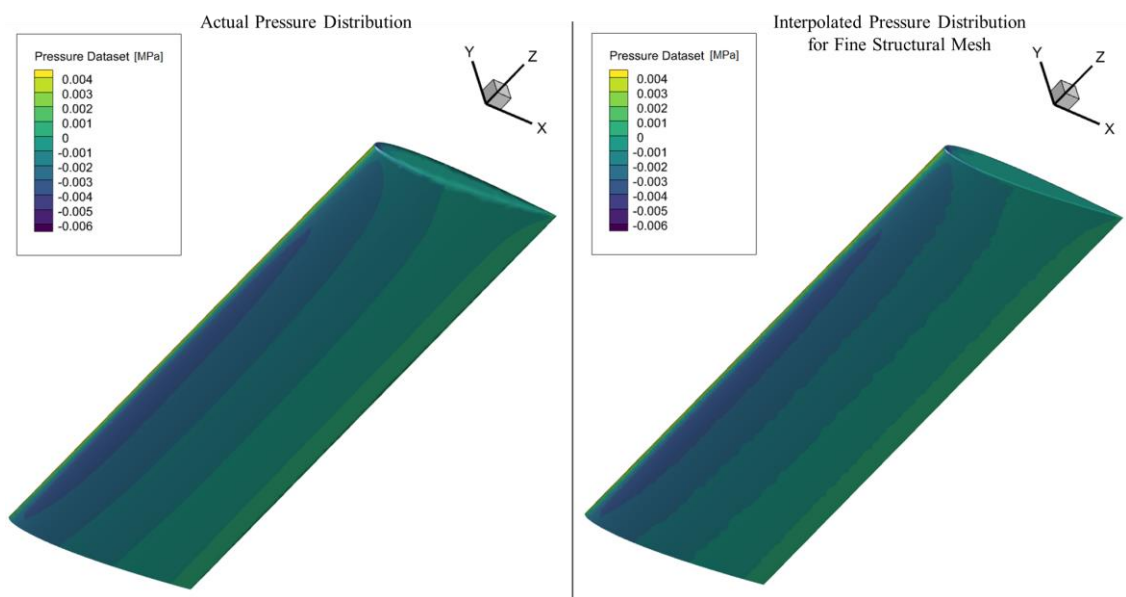
Figure 4.10 Comparison of Actual Pressure with Interpolated Pressure for Fine FE Mesh on the Lower Skin

Similarly, the actual pressure distribution on the lower skin is compared with the interpolated pressure distribution for coarse structural mesh in Figure 4.11 and Figure 4.12.
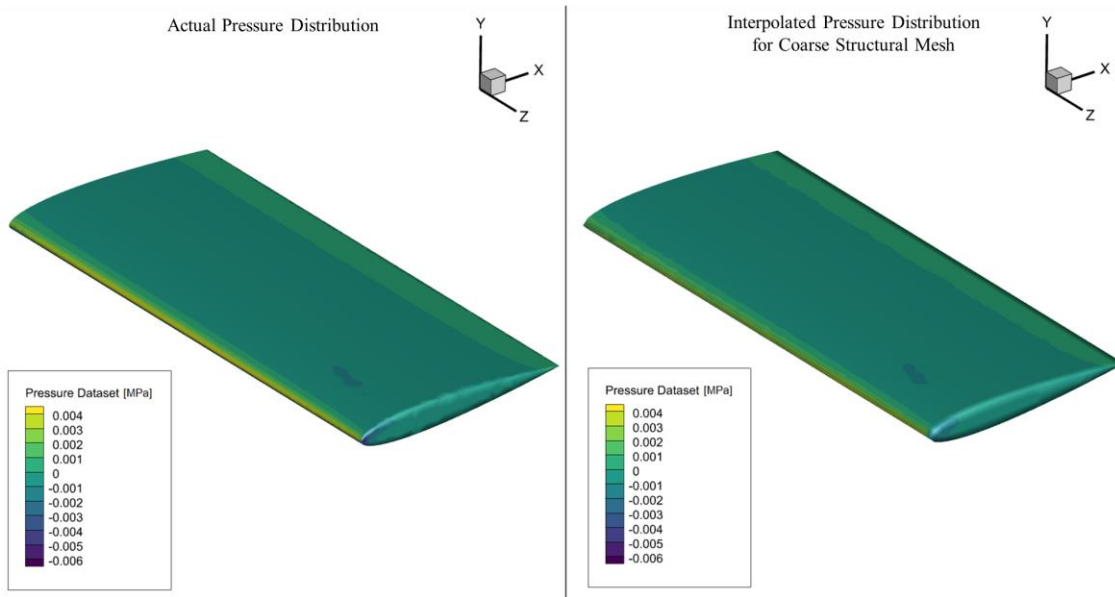
Figure 4.11 Comparison of Actual Pressure with Interpolated Pressure for Coarse FE Mesh on the Upper Skin
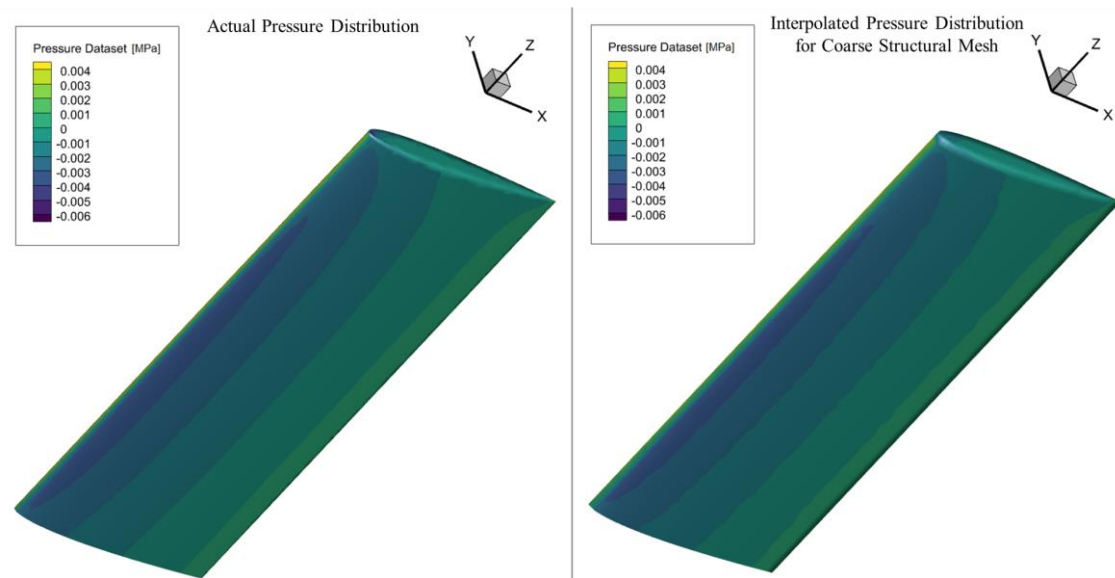
Figure 4.12 Comparison of Actual Pressure with Interpolated Pressure for Coarse FE Mesh on the Lower Skin

Figure 4.13 and Figure 4.14 show the comparison between the actual pressure and interpolated pressure at the wing tip and the leading edge for the fine and coarse structural mesh, respectively.
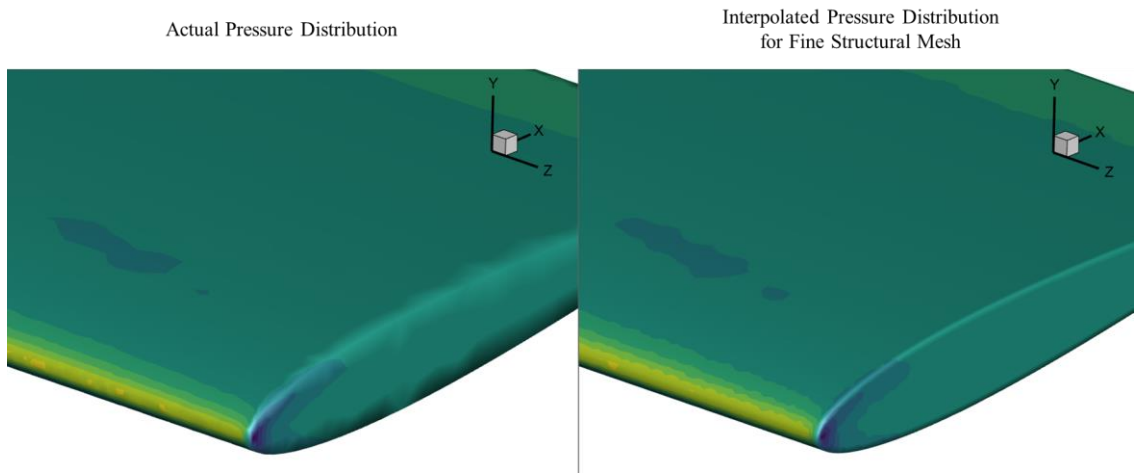
Figure 4.13 Comparison of Actual Pressure with Interpolated Pressure for Fine FE
Mesh at the Wing Tip
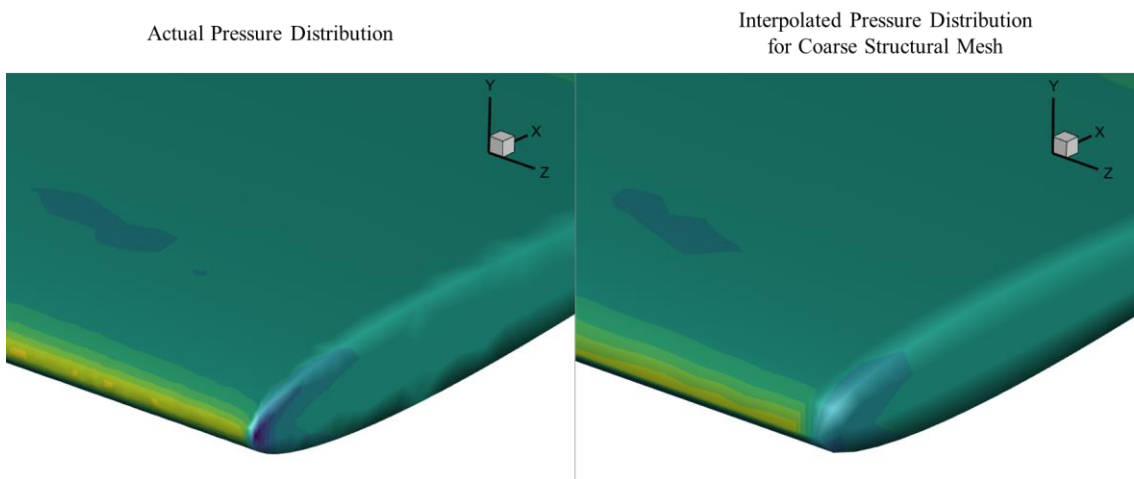
Figure 4.14 Comparison of Actual Pressure with Interpolated Pressure for Coarse FE
Mesh at the Wing Tip

It is obvious that the model with the fine mesh captures the real pressure pattern better
than the model with the coarse mesh.

4.4. Finite Element Modelling and Analysis of the Horizontal Stabilizer

In this part, the finite element model (FEM) of the horizontal stabilizer is prepared using HyperMesh, a finite element pre-processor of Altair HyperWorks [56]. The process of creating the FEM is shown in this section for the stabilizer with three internal ribs. Moreover, the study of modelling and analysis of other stabilizer configurations is also included in the thesis to train the ANN model, even though it is not explicitly shown.

4.4.1. Material Properties

Before meshing the model, component materials must be defined. Aluminum alloys are lightweight materials commonly used in aerospace structures due to their comparatively high stiffness, specific strength, corrosion resistance, ease of manufacturing, and low costs [48-49]. Therefore, aluminum alloys will be the material choice for the components.

Spars are generally designed as I-section machined parts since they are subjected to bending and shear stresses. In this way, the spar web carries the shear stress while the spar flanges carry the bending stress. 7050 aluminum alloys are widely used in highly loaded components such as bulkheads and frames [57]. Therefore, 7050 T7451 aluminum alloy is chosen as the spar material. Ribs are sheet metal parts that are formed by hydro press manufacturing and treated with heat. Skin is made of a sheet metal which does not need any additional heat treatment. They are both designed to withstand damage by foreign objects [59]. 2024 aluminum alloys are also common aerospace structure materials due to their good fatigue and damage tolerance characteristics [57]. So, 2024 T42 and 2024 T3 aluminum alloys have been selected as rib and skin materials, respectively.

The material allowables of the aluminum alloys used in FEM are given in Table 4.1.

Table 4.1 Material Allowables of the Aluminum Alloys [60]

	2024 T3 Clad	2024 T42 Clad	7050 T7451
Young's Modulus, E [GPa]	72.4	72.4	71
Poisson's Ratio, v	0.33	0.33	0.33
Tensile Ultimate Strength, F_{tu} [MPa]	406.8	393	510.2
Tensile Yield Stress, F_{ty} [MPa]	268.9	234.4	441.3
Compressive Yield Stress, F_{cy} [MPa]	248.2	255.1	427.5

The thickness of the components should also be defined in FEM as a property. In this part of the analysis, spar web and spar flange thicknesses are 2.5 mm, whereas rib, rib flange, and skin thicknesses are assigned 1.27 mm. These are the nominal values used in the training of the ANN model.

4.4.2. Finite Element Modelling

The geometry required for the modelling has already been created as shown in Figure 4.3. The meshed model of the wing can be created using this geometry. In this part, the wing is modelled using 1D and 2D elements only to reduce the number of elements as well as the computation time. Therefore, the skin, ribs, and spar webs are meshed using 2D shell elements. Furthermore, the flanges of the ribs and spars are modelled using 1D elements. There are three different 1D element types, CROD, CBAR, and CBEAM. CROD elements carry only tension and compression, while CBAR and CBEAM elements resist bending additionally. CBAR elements are the simplified version of CBEAM elements. They are preferred to model the geometries having a symmetrical cross-section. Contrarily, complex geometries having various cross sections are modelled using CBEAM elements. Hence, CBAR elements are implemented to model the flanges of spars and ribs since they possess constant symmetrical cross-sections. Moreover, the mesh model of the wing with an 8 mm mesh size can be seen in Figure 4.15.
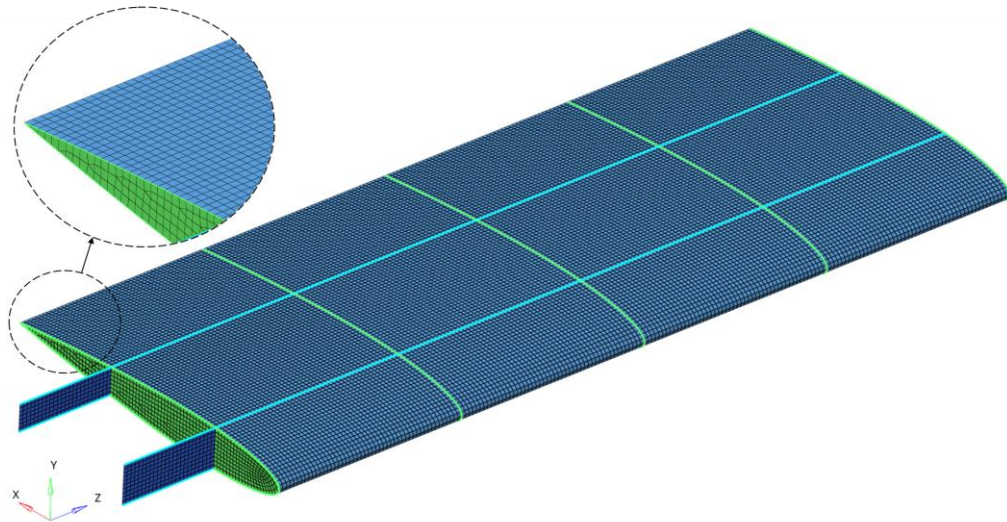
Figure 4.15 The Mesh Model of the Wing with an 8 mm Mesh Size

The mesh model without the skin is shown in Figure 4.16. The spar flanges and the rib flanges are represented by turquoise-colored elements and light green-colored elements, respectively.
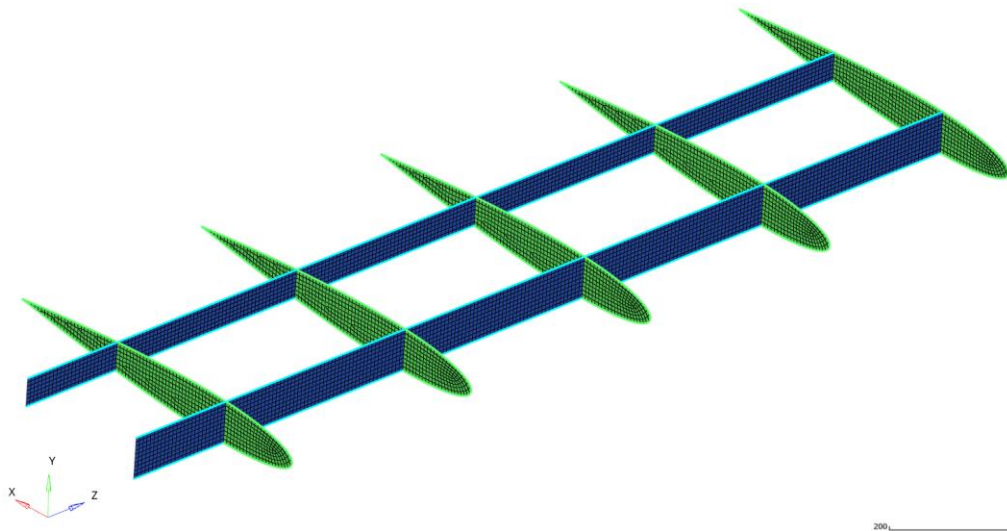
Figure 4.16 The Mesh Model of the Wing without the Skin

The cross-section of the flanges is specified as a standard rectangular solid in the model. In addition, the sizing of the flanges is determined through the connection concept as shown in Figure 4.17.
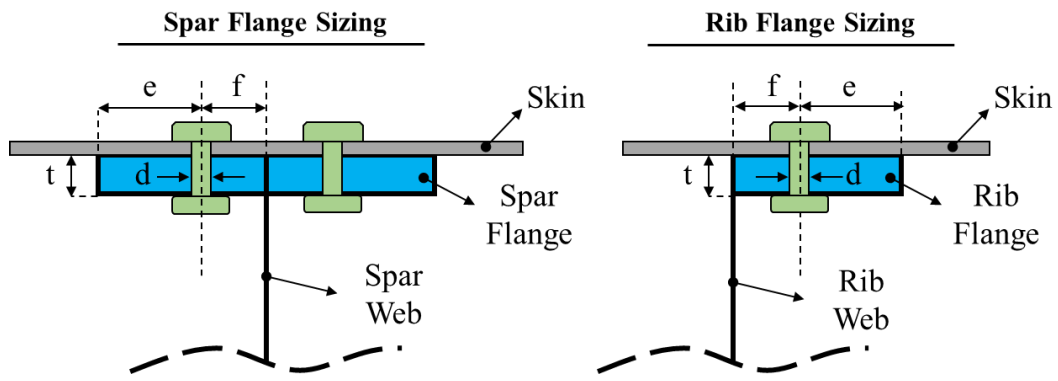
Figure 4.17 The Flange Sizing

As illustrated in Figure 4.17, spars are I-section beams having two lateral symmetric flanges, whereas ribs are sheet metal parts with bent flanges. These flanges are attached to the skin through aluminum rivets. These rivets used in airframe joints should have a minimum diameter of 5/32 inches [61]. Therefore, the flange sizes can be calculated using this diameter. The minimum edge distance of the fastener (e) is two times the fastener diameter, d plus 0.03 inch [51, 53]. The fillet spacing (f) can be approximated as the fastener diameter, d plus 0.03 inch, as a rule of thumb in the industry. Lastly, t indicates the flange thickness defined in the model as a property. Therefore, the sizing of the flanges is determined using these rules. The internal structure model with the 3D representation of the flanges is shown in Figure 4.18.
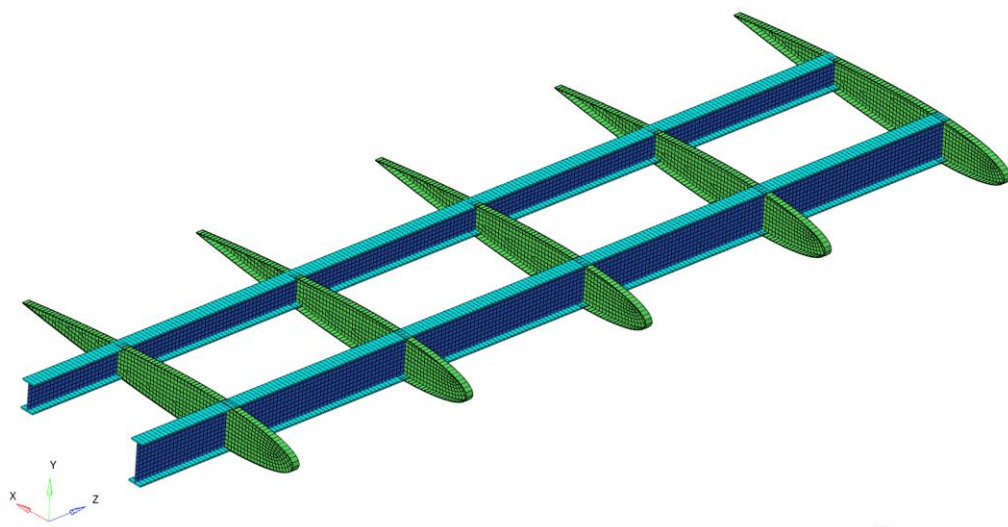
Figure 4.18 The Model with the 3D Representation of the 1D Elements

4.4.3. Loads and Boundary Conditions

The pressure load determined through the CFD analysis is interpolated onto the structural mesh. Then, it is implemented over the wing as a load after checking the surface normals. Moreover, the wing roots are fixed in x, y, and z translational directions as a displacement boundary condition. The rotations become fixed in this case since there are two spars. The loads and boundary conditions applied on the wing are shown in Figure 4.19.
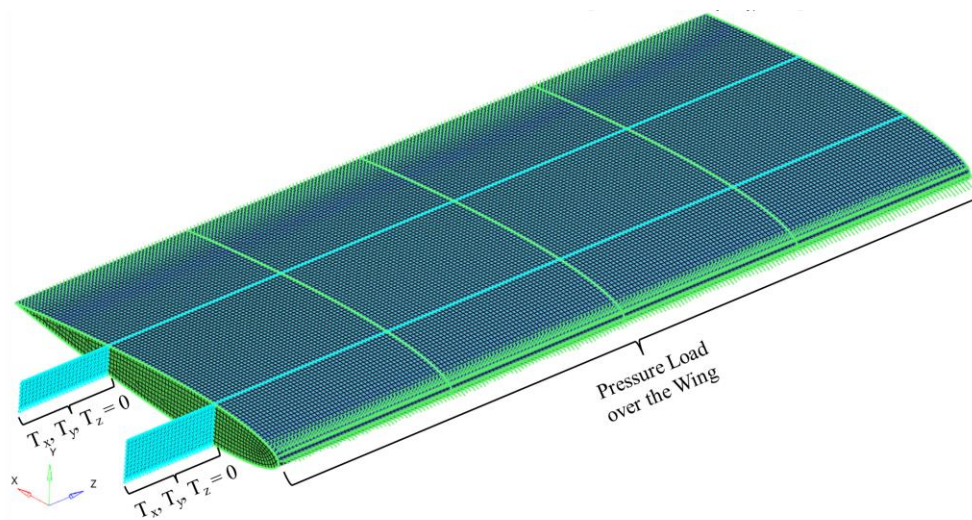
Figure 4.19 The Loads and Boundary Conditions

A detail view of the loads and boundary conditions is given in Figure 4.20.
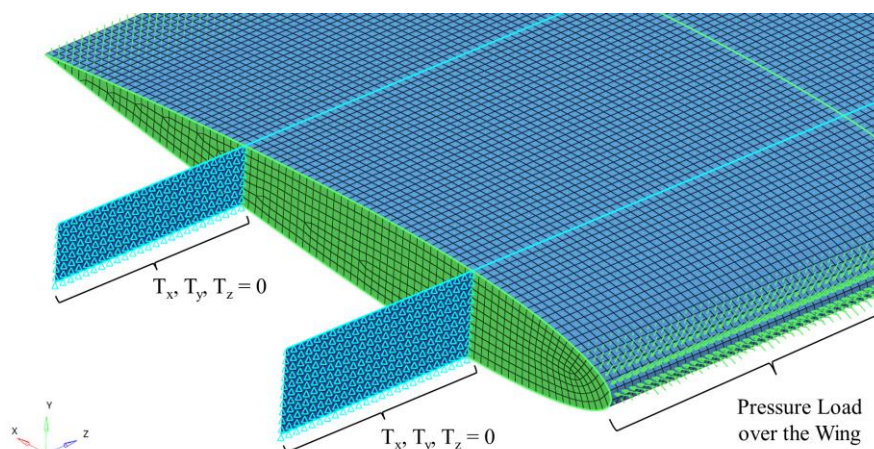
Figure 4.20 A Detail View of Loads and Boundary Conditions

On the middle area of the skin, the pressure load vector points outwards inside the skin because the vector ends on the skin surface. However, if the vector is positioned such that it starts on the skin surface, the loads not visible in Figure 4.20 become apparent in Figure 4.21.
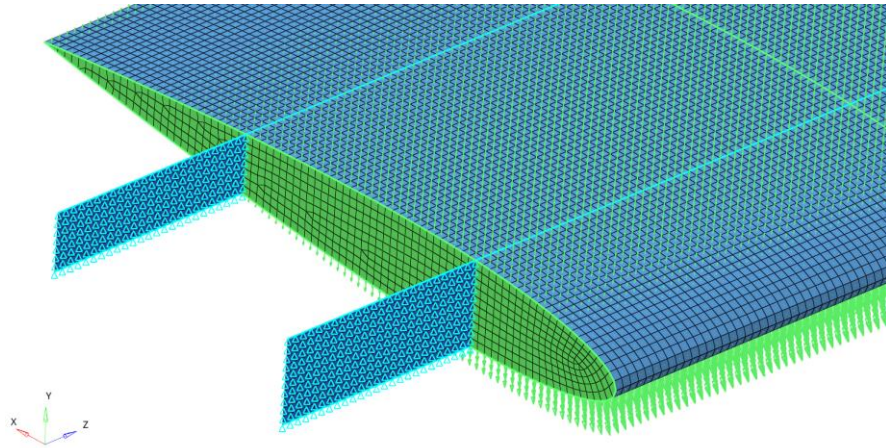
Figure 4.21 The Load Vectors Starting on the Skin

4.4.4. Mesh Convergence Study

Although the smaller mesh sizes produce more precise results, they increase the computational cost and time. Therefore, it is significant to select the optimum mesh size for the finite element in order to balance the accuracy and the cost. In the previous section, the wing model was created with a mesh size of 8 mm. In this part, the wing is modelled with different mesh sizes to reach the optimum mesh size. The additional wing models with 5, 10, 25, and 50 mm mesh sizes are shown in Figure 4.22, Figure 4.23, Figure 4.24, and Figure 4.25, respectively.
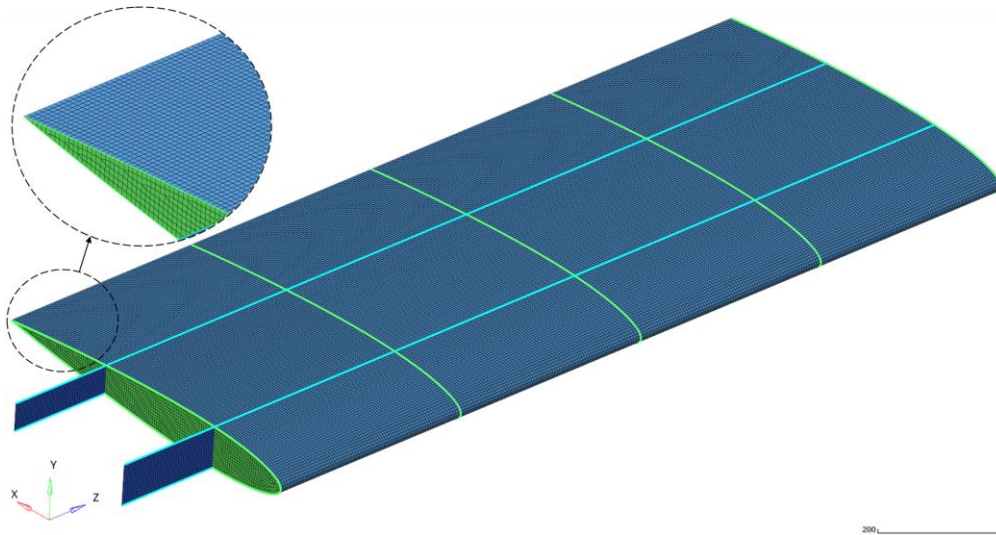
Figure 4.22 FEM of the Wing with a Mesh Size of 5 mm
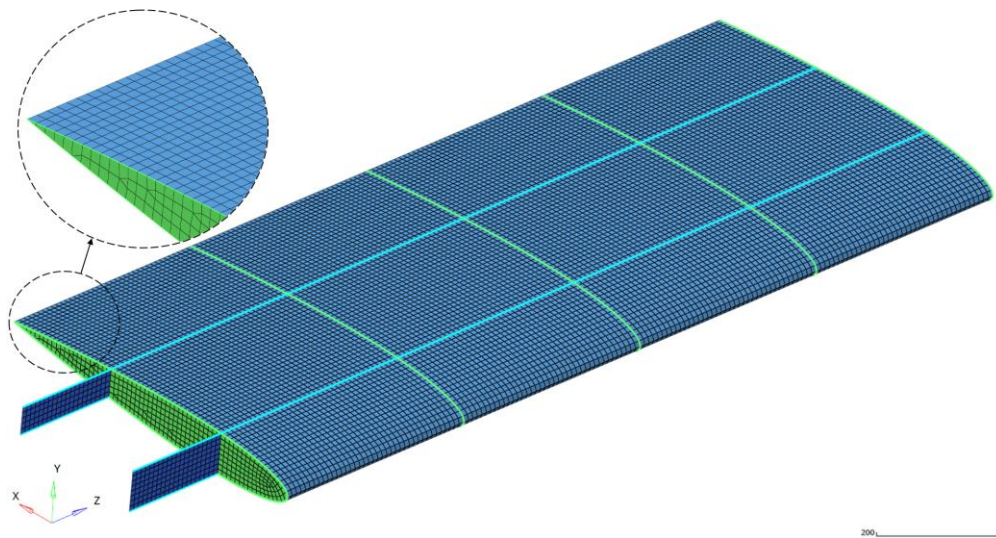
Figure 4.23 FEM of the Wing with a Mesh Size of 10 mm

As the mesh size increases, the model does not manage to capture the leading edge of the actual wing geometry as indicated in Figure 4.24 and Figure 4.25. As discussed before, the interpolated pressure pattern gets worse as well.
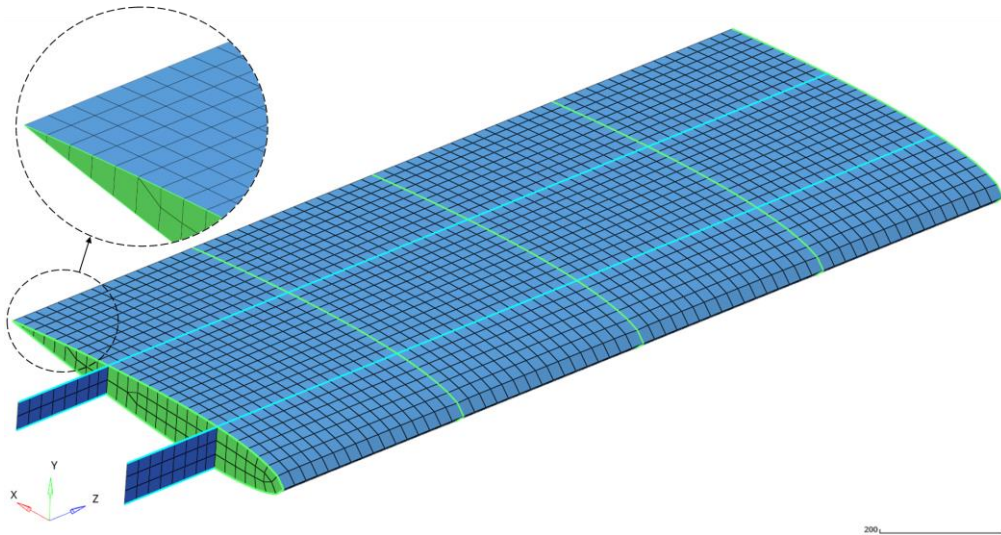
Figure 4.24 FEM of the Wing with a Mesh Size of 25 mm
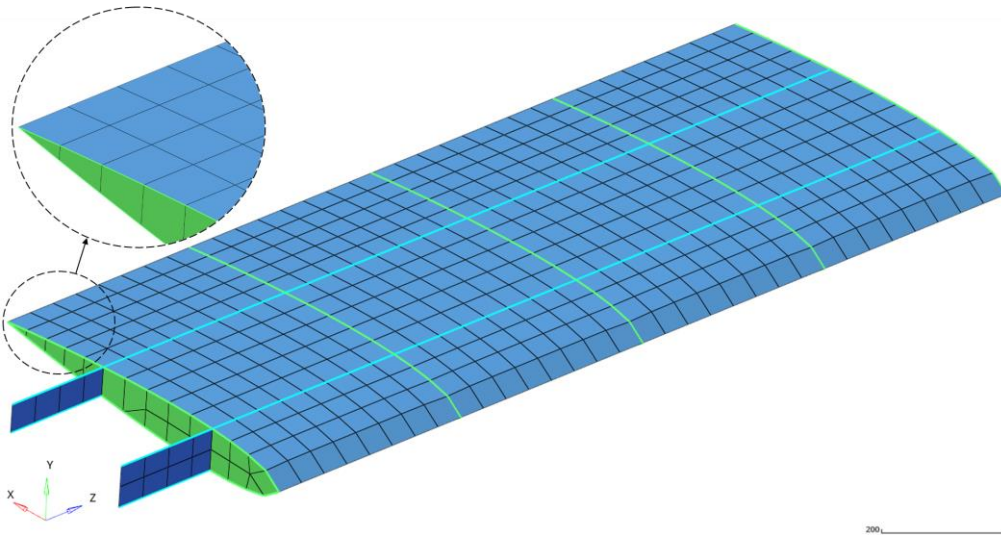
Figure 4.25 FEM of the Wing with a Mesh Size of 50 mm

Wing models with five different mesh sizes are analyzed given the material properties and load boundary conditions. The maximum tip displacements are then compared. Figure 4.26 shows that the maximum tip displacement converges around 4.15 mm. The results close to this value are obtained for the wing models with 5, 8, and 10 mm mesh sizes.
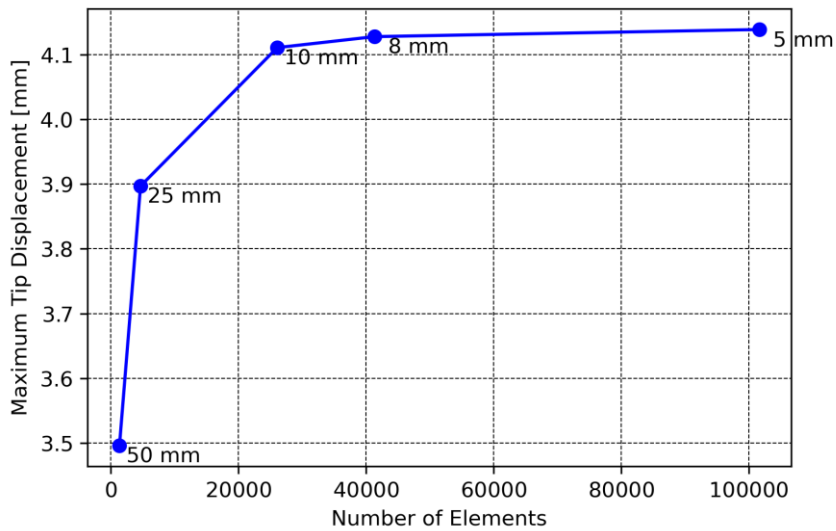
Figure 4.26 Maximum Tip Displacement vs. Number of Elements

Figure 4.27 shows the number of elements with the corresponding mesh size. It is seen that the model with a 5 mm mesh size consists of approximately 100,000 elements. Moreover, the model with an 8 mm mesh size includes around 40,000 elements, with a 60% decrease. The number of elements for 8 mm and 10 mm mesh sizes is relatively close. In conclusion, an 8 mm mesh size is chosen since it gives a promising result with a smaller number of elements.
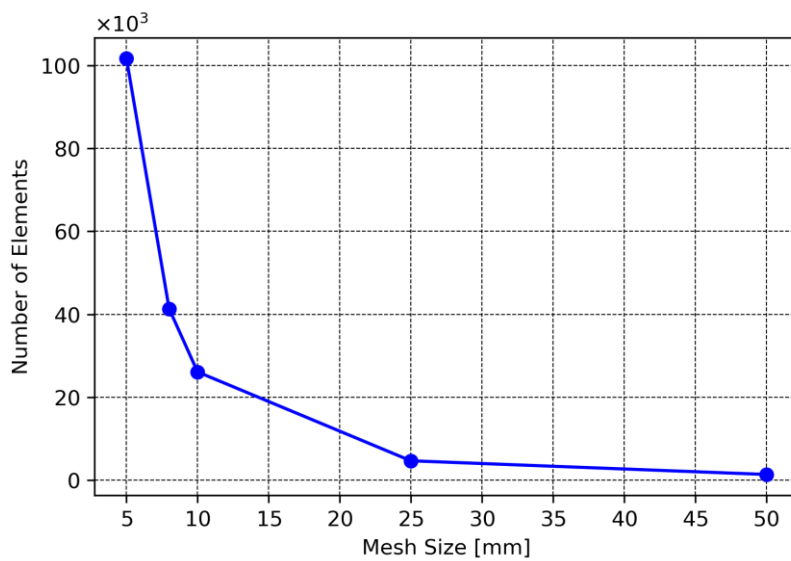
Figure 4.27 Number of Elements vs. Mesh Size

The analysis results will be given and discussed for the prepared model in the following section. Since the materials of the structural components are ductile, the von Mises or the Tresca failure criterion can be selected to observe if the yielding occurs. In comparison with the von Mises criterion, Tresca is a more conservative failure theory. However, it may require taking unnecessary actions to avoid improbable failure. On the other hand, von Mises is a commonly used criterion since it is more consistent with the experimental data [21, 54]. Therefore, the von Mises criterion will be implemented in the analysis.

4.4.5. Results and Discussion of the Finite Element Analysis

The horizontal stabilizer is analyzed using OptiStruct, an analysis solver of Altair HyperWorks. The loads and boundary conditions are presented in Figure 4.19. Moreover, the analysis is performed for the model with a mesh size of 8 mm.

The total displacement plot of the horizontal stabilizer is given in Figure 4.28. Accordingly, the maximum tip displacement is obtained as 4.128 mm. As mentioned before, the stabilizer generates a negative lift to oppose the pitch behavior of the rotor. Figure 4.28 shows this behavior such that the stabilizer deflects downwards under the aerodynamic load, as expected.
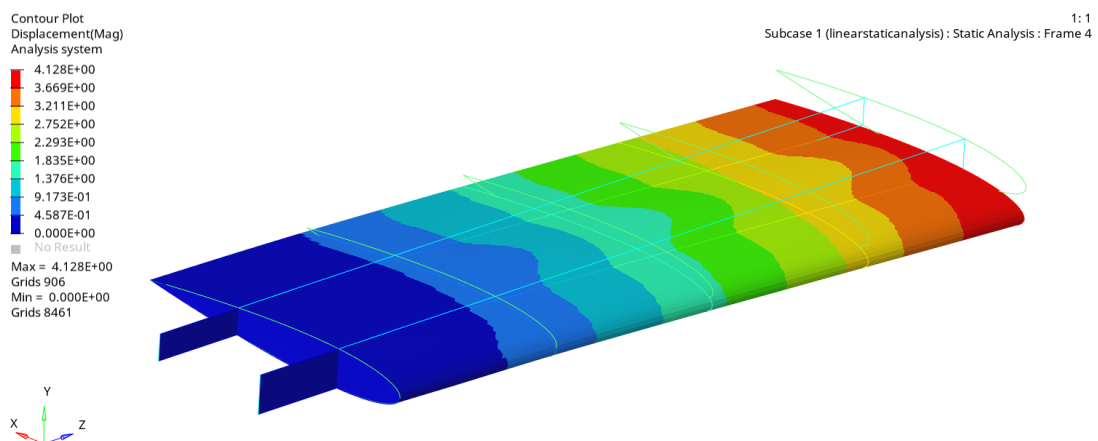
Figure 4.28 The Total Displacement of the Wing Model

The von Mises stress plot is presented for the entire wing in Figure 4.29. The von Mises stress increases towards the wing root. As given previously, the front spar was located at 25% of the chord since the center of pressure and the aerodynamic center are at the quarter-chord point of a symmetric airfoil. As anticipated, the maximum von Mises stress is obtained around the intersection of the front spar with the root rib with 51.34 MPa. In this case, the stabilizer does not yield since the yielding stresses are much higher.
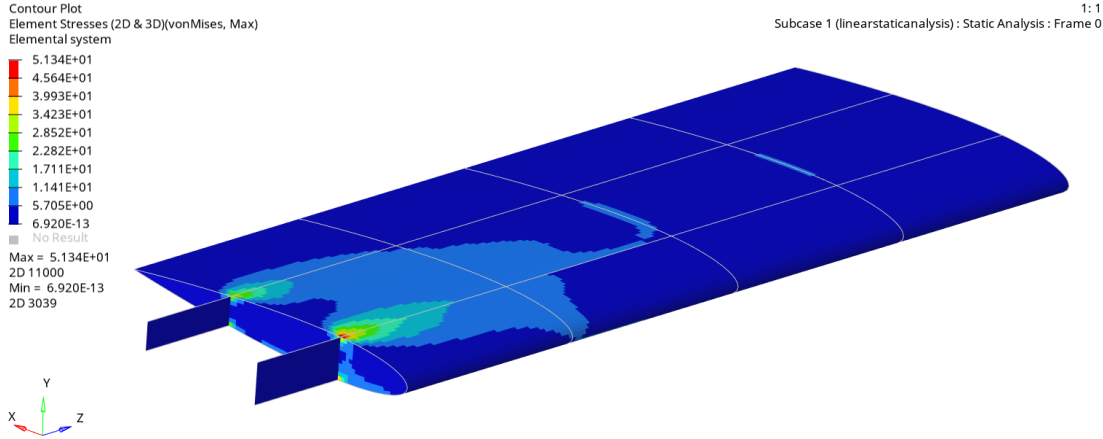
Figure 4.29 The Von Mises Stress Plot of the Wing Model

The von Mises stress plots can be created for each component. Figure 4.30 shows the von Mises stress contours of the skin. The maximum equivalent von Mises stress is obtained around the front spar at the root with 51.34 MPa.
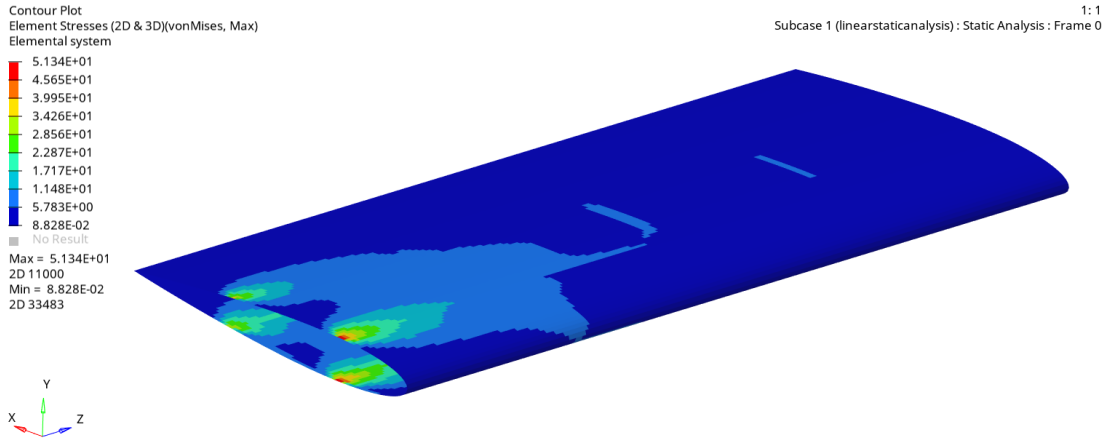
Figure 4.30 The Von Mises Stress Plot of the Skin

Similarly, the von Mises stress plot of the spar webs is depicted in Figure 4.31. The maximum equivalent von Mises stress is determined at the root of the front spar with 34.32 MPa.
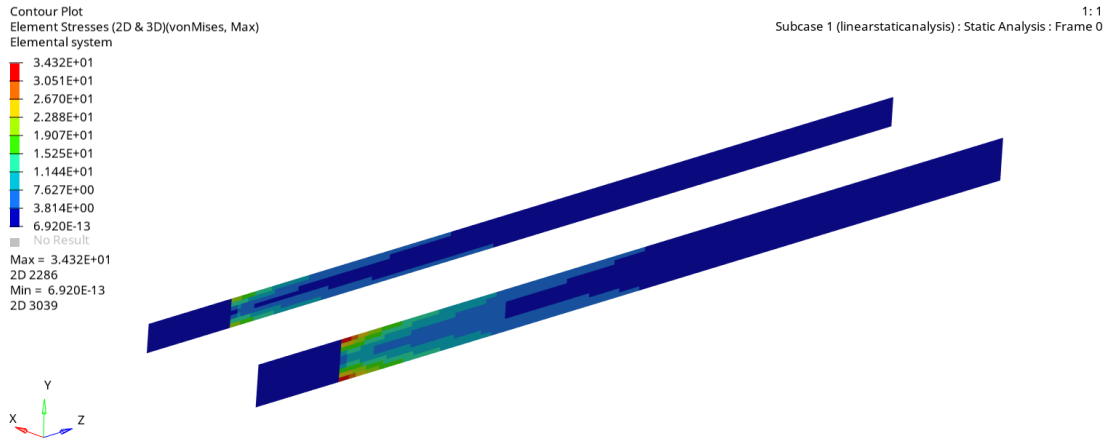
Figure 4.31 The Von Mises Stress Plot of the Spar Webs

Furthermore, Figure 4.32 shows the von Mises stress plot of the rib webs. The maximum equivalent von Mises stress is calculated at the intersection of the root rib with the front spar with 35.95 MPa.
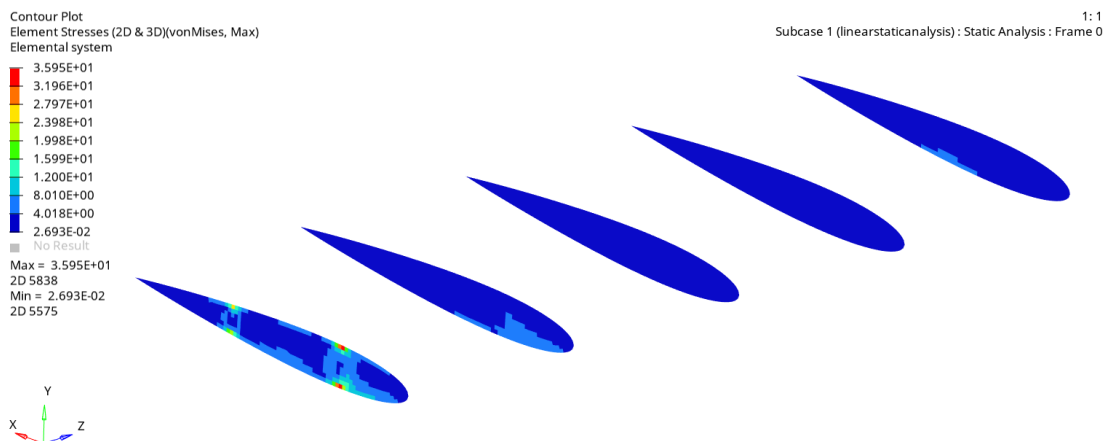
Figure 4.32 The Von Mises Stress Plot of the Rib Webs

It is possible to observe the axial stresses on the flanges. Figure 4.33 and Figure 4.34 present the axial stresses on the spar flanges and rib flanges, respectively.
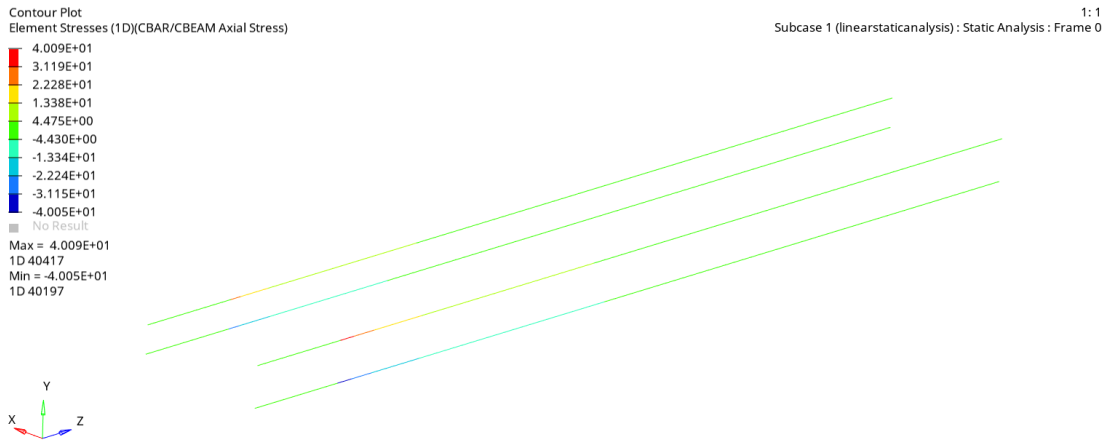
Figure 4.33 The Axial Stress Plot of the Spar Flanges

The maximum axial stress on the spar flanges occurs at the root of the front spar. Moreover, it can be seen that tensile stress occurs on the upper flanges, while compressive stress acts on the lower flanges.

Finally, the axial stress plot of the rib flanges is given in Figure 4.34. Accordingly, stress levels increase towards the root rib and become maximum on the root rib.
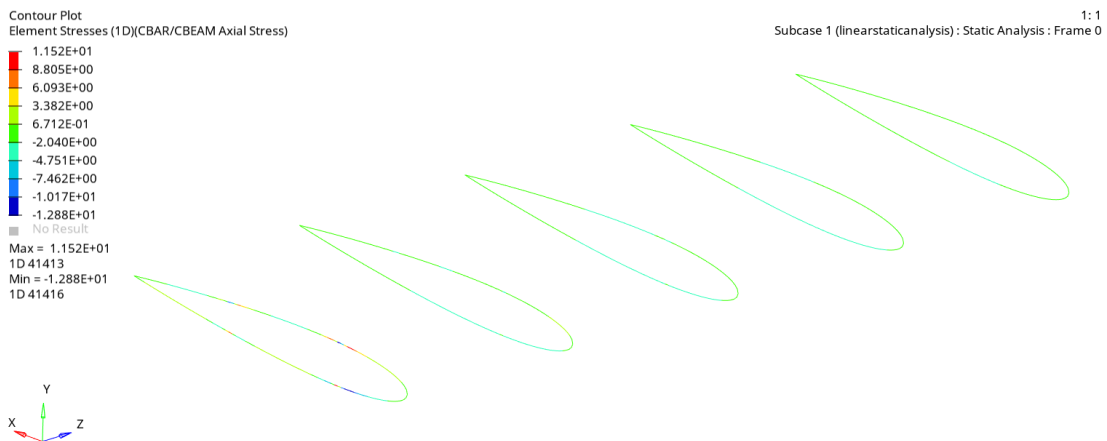
Figure 4.34 The Axial Stress Plot of the Rib Flanges

5. ARTIFICIAL NEURAL NETWORKS

In this section of the thesis, the construction of the ANN model is explained based on the theoretical background described in the previous sections. As mentioned before, NNs learn from experiences and need many data. Therefore, a database will be created first for the training of the ANN model. FEA results will be utilized to build this database. Next, the ANN will be modelled using Python programming language. Finally, the model's performance will be monitored to check if the model is appropriately established.

The general structure of the ANN model is depicted in Figure 5.1.
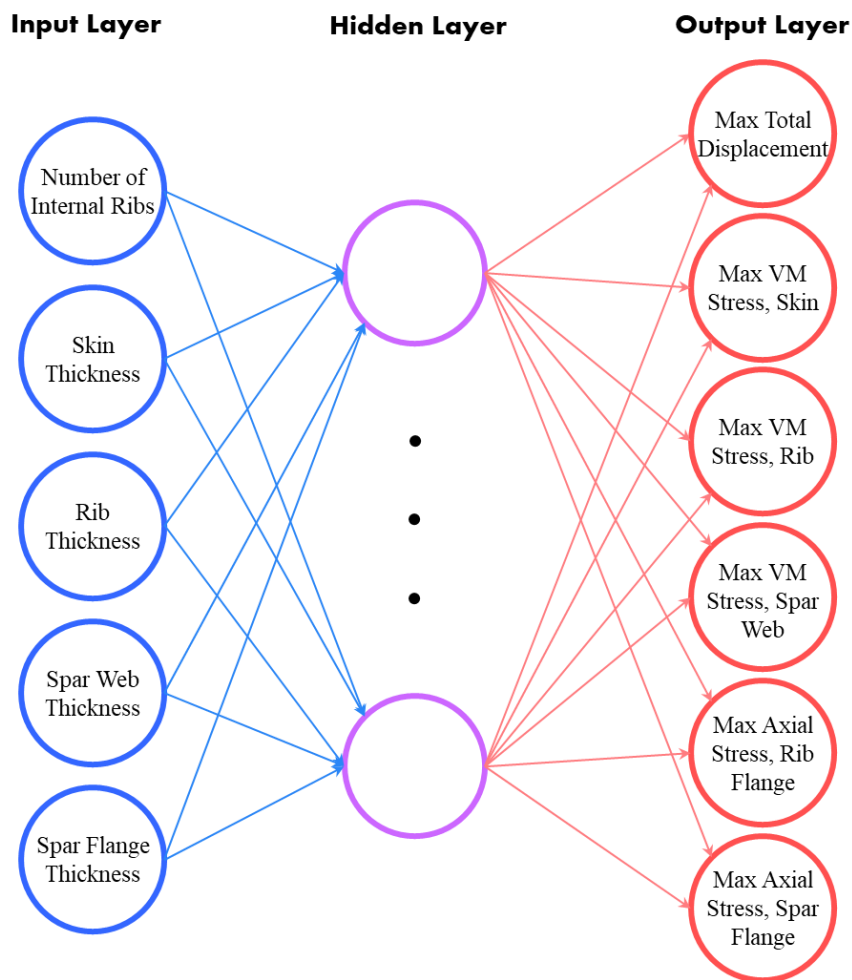
Figure 5.1 Inputs and Outputs of the ANN Model

The model uses five design variables as inputs: the number of internal ribs, skin thickness, rib thickness, spar web thickness, and spar flange thickness. Besides, these variables do not change the stabilizer's master geometry. After processing the data through a hidden layer, the model outputs the maximum total displacement of the wing, the maximum von Mises stresses on the skin, rib, and spar web, and the maximum axial stresses on the rib flange and the spar flanges.

Since the spars are modelled as I-beams with the same flange areas, almost equal tension and compression are obtained on the flanges. Therefore, the tensile and compressive yield stresses can be checked according to the maximum axial stress on the spar flanges. In addition, the tensile yield stress of the rib material, 2024 T42 aluminum alloy, is lower than the compressive yield stress. Therefore, the tensile stress on the rib flanges is more critical than the compressive stress in terms of yielding. For this reason, the tensile yield stress of the rib material can be controlled according to the maximum axial stress on the rib flanges.

5.1. Data Generation and Preparation for the Model

In this part, the required database will be created to train the model. As explained before, NNs are trained using the data including inputs and corresponding targets. Firstly, the values for the input variables are assigned as given in Table 5.1. There are three internal rib configurations, as described before. The skin and ribs are made of sheet metals. The values for these members were chosen considering commonly used sheet metal thicknesses in the industry. On the other hand, spars are machined parts. Therefore, typical thicknesses were assigned separately for the web and flange of the spar.

Table 5.1 Input Variables

The Number of Internal Ribs	2, 3, 4
Skin Thickness [mm]	0.51, 0.81, 1.27, 1.6, 2.03
Rib Thickness [mm]	0.51, 0.81, 1.27, 1.6, 2.03
Spar Web Thickness [mm]	1.5, 2, 2.5, 3, 3.5
Spar Flange Thickness [mm]	1.5, 2, 2.5, 3, 3.5

The full factorial design is constituted by all possible combinations of the input variables. Therefore, it requires 1875 analyses (3×5^4) to determine the targets. Instead of performing analyses manually, the analysis procedure can be automated using Hyperstudy, Altair HyperWorks's design space exploration tool [56].

After the FEM is generated, HyperMesh creates a ".fem" file for the solver. This file consists of information about the FEM. HyperStudy allows the conversion of this file into a parameterized file. The input variables and the affected dependents are defined in this parameterized file. By assigning the values of input variables in the program, the analyses are performed automatically. As a result of the analyses, ".h3d" result files are generated, and the desired outputs are extracted from these files. This process is repeated for each rib configuration of the wing, and the information obtained is gathered in a CSV (Comma-Separated Values) file to import into Python using the Pandas library. Resultantly, the database becomes ready for the ANN model.

The generated data consists of values with different orders of magnitudes, such as thicknesses in mm and stresses in MPa. Therefore, the data should be normalized to enhance the training quality [63]. The mathematical formula for normalization is given by Equation (5.1).

$$x_n = \frac{x - x_{min}}{x_{max} - x_{min}} \qquad (5.1)$$

After the data is normalized, it needs to be divided into three data groups to tune the hyperparameters of the network. These are training, validation, and test groups. The dataset is split into 70% for the training set, 15% for the validation set, and 15% for the test set [37]. The "train_test_split" function of the Scikit-learn library is employed for this operation. As the name suggests, the training set is utilized for training the model and adjusting weights and biases. The validation set is used to evaluate the model fit. These groups have an impact on the model. However, the test set is used to monitor the model's performance and does not affect the training phase.

5.2. ANN Modelling

The model is constructed using the Keras library. Firstly, a sequential model is defined in the code environment. Next, ReLU is chosen as an activation function, and Adam is picked as a backpropagation training algorithm by considering the theory. Furthermore, the cost function is assigned as MSE. Although the maximum number of epochs was specified as 5000, the early stopping criterion was defined to avoid the overfitting problem. Accordingly, the program monitors the validation and the training error as depicted in Figure 5.2.
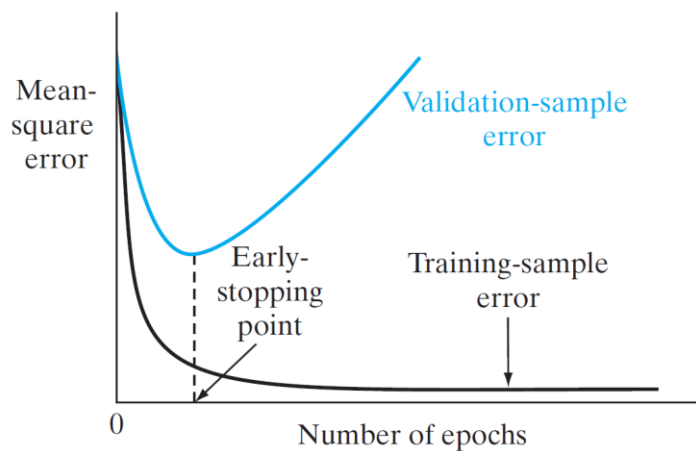
Figure 5.2 The Early Stopping Criterion [32]

If the validation error starts to increase after getting to its minimum, training stops after some patience. "Patience" is defined to investigate if the validation error still tends to decrease. Therefore, patience is decided as 50 epochs.

The neural network architecture should also be defined to complete the model. As discussed before, a single hidden layer solves most fitting problems. Hence, a single hidden layer is assigned between the input and output layers. Moreover, the number of neurons in the hidden layer can be determined through the trial-and-error approach. As exhibited in Figure 5.3, ANN models are built for a different number of neurons, and mean squared errors for each finalized model are compared. Increasing the number of neurons decreases the MSE as expected.
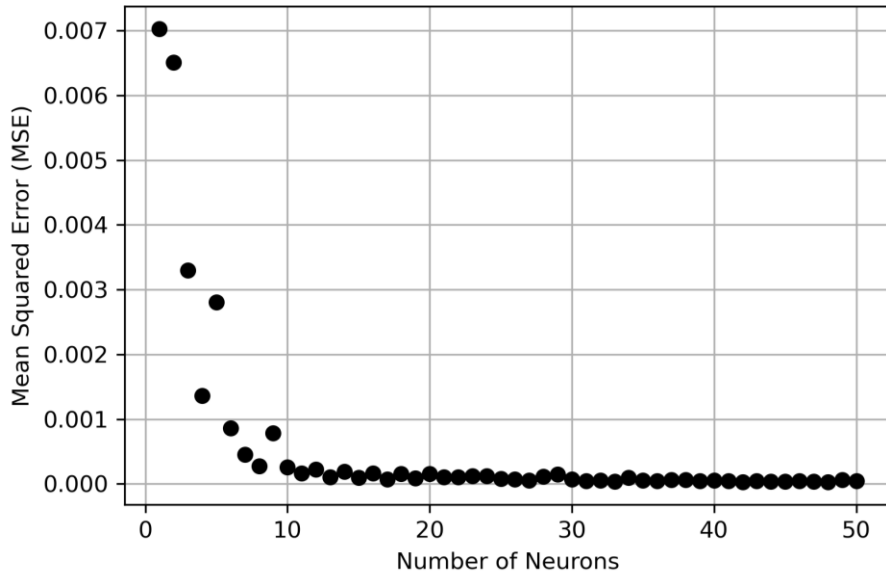
Figure 5.3 MSE vs. Number of Neurons

The graph was also presented in logarithmic scale in Figure 5.4 to analyze the situation better. Accordingly, the model with 48 neurons in the hidden layer gives the minimum error. However, in order to decrease the model complexity, the model with 33 neurons in the hidden layer is selected since it gives almost the same error.
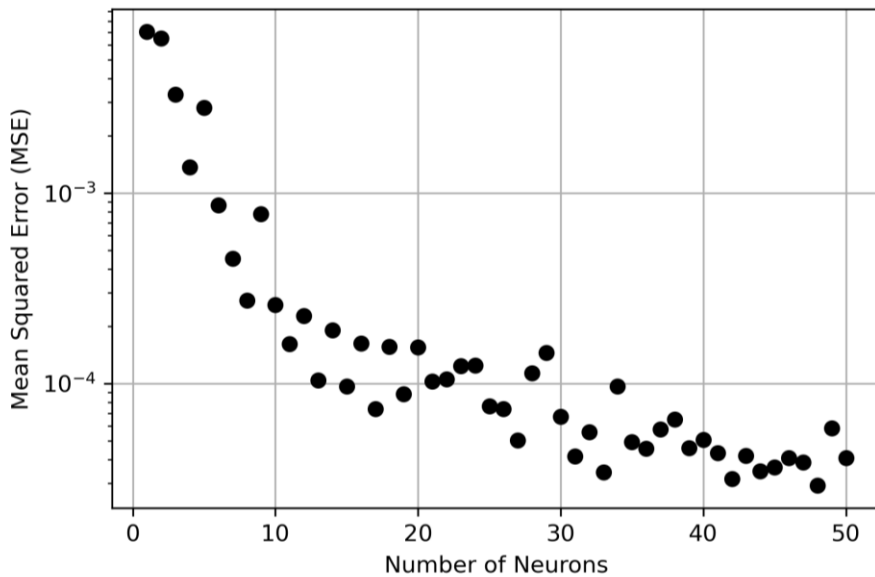
Figure 5.4 MSE vs. Number of Neurons in Logarithmic Scale

Lastly, the model outputs will be obtained as normalized since the data is initially normalized. Therefore, after the outputs are obtained, they are denormalized to get the actual value.

5.3. Performance of the Model

The model is built and trained with the hyperparameters defined and the data generated previously. The model loss during the training of the constructed model is presented in Figure 5.5. As shown in the figure, the model loss reduces as the model gets trained and converges to a pretty small value. The training stops in the 545th epoch with early stopping even though the maximum number of epochs is specified as 5000.
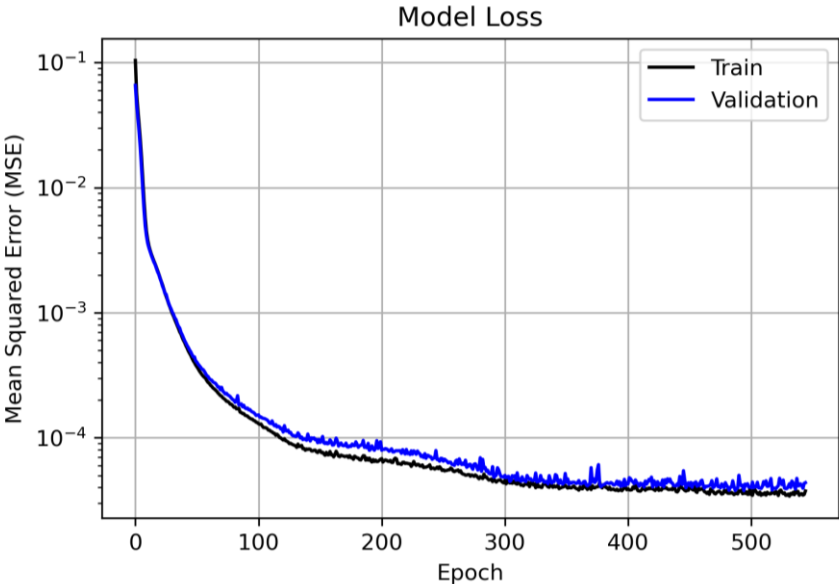
Figure 5.5 Model Loss vs. Epochs in Log Scale

The regression plots are given individually in Figure 5.6, Figure 5.7, and Figure 5.8 for the training, validation, and test data, respectively. The red line in the figures represents where the output is equal to the target. As seen from the figures, the points are obtained close to this curve. Besides, the "R" value above the graphs corresponds to the Pearson correlation coefficient. The correlation between the outputs and the targets is very high according to the correlation coefficients calculated.
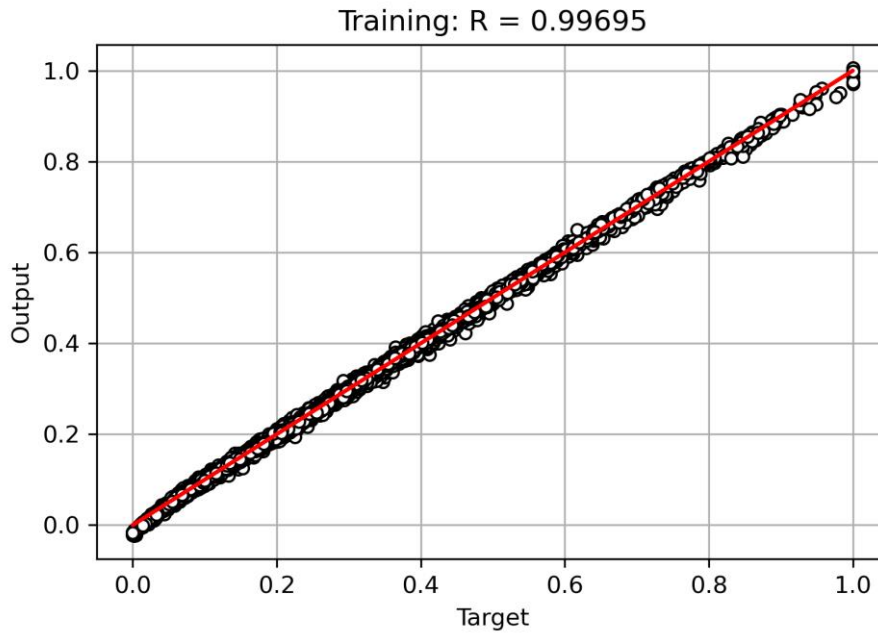
Figure 5.6 Regression Plot for the Training Data
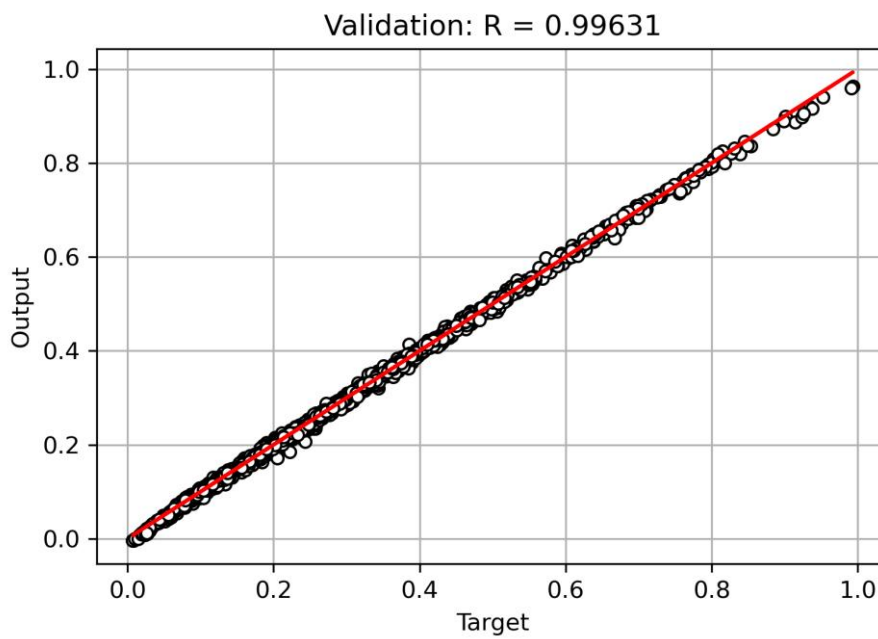
Figure 5.7 Regression Plot for the Validation Data
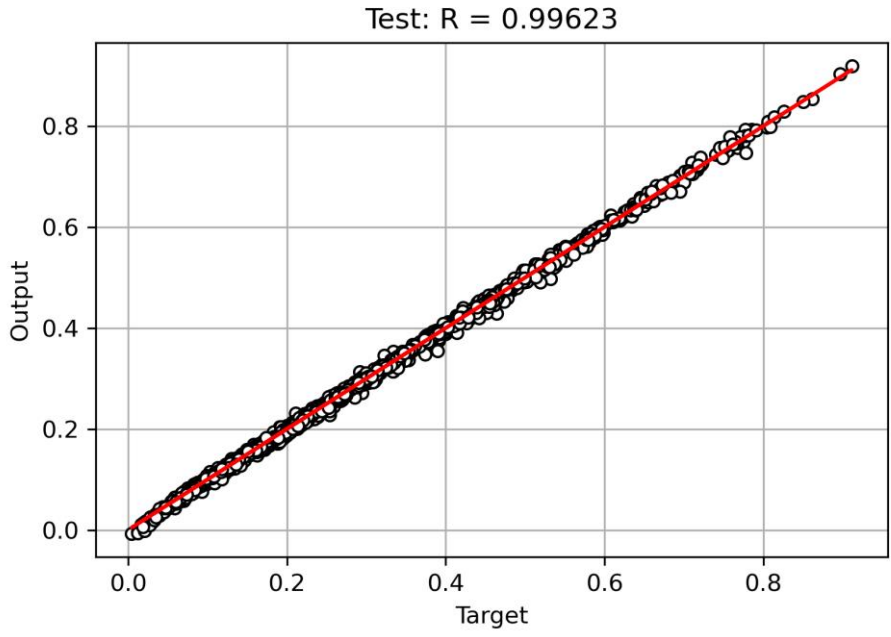
Figure 5.8 Regression Plot for the Test Data

The regression plot can also be drawn for the overall data as depicted in Figure 5.9. Considering the correlation coefficient and the model loss, the model's performance is outstanding.
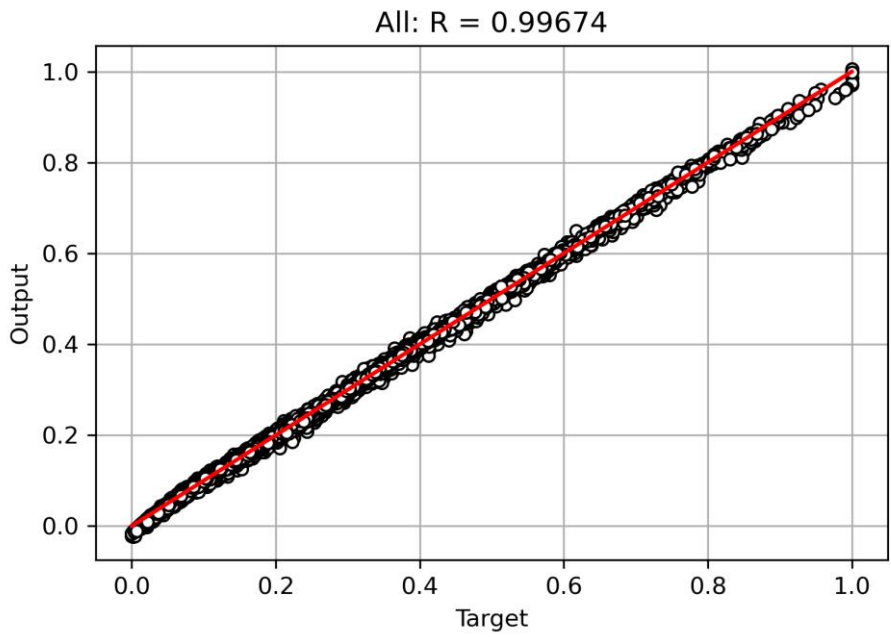
Figure 5.9 Regression Plot for the Entire Data

5.4. Results and Discussion

This section presents the results of the ANN-based design tool for the horizontal stabilizer of a helicopter. Firstly, the estimation accuracy of the ANN model is shown for the full factorial design input. Then, several additional samples are created to evaluate the ANN model's performance for different cases. The output of the model with the full factorial design is compared with the FEA results using these samples. Finally, the effect of decreasing the number of data feeding the network model is assessed. In this context, the input data is reduced to 75% and 50% of the initial data through Hammersley sampling. Accordingly, the results of the ANN model with 75% and 50% of the full factorial design are presented.

5.4.1. ANN Generation with the Full Factorial Design Input

In this section, the ANN model with the full factorial design will be examined. First of all, 1875 analyses were performed, and the results were introduced into the model to make predictions. Then, the regression plot of the model was obtained as shown in Figure 5.9. According to the plots, the correlation coefficient of the model was determined as 0.99674. In order to evaluate the model's accuracy better, the data distribution percentile according to the percentage error ranges is tabulated in Table 5.2 for the input data.

Table 5.2 Accuracy of the ANN model with the Full Factorial Design Input

| Percentage Error | Data Distribution Percentile [%] | | | | | |
| | Max Total Displacement | Max Von Mises Stress | | | Max Axial Stress | |
		Skin	Rib	Spar Web	Rib Flange	Spar Flange
< 3%	99.4	99.3	99.9	99.8	96.1	99.8
3% - 5%	0.6	0.7	0.1	0.2	3.4	0.2
5% - 10%	0.0	0.0	0.0	0.0	0.5	0.0
> 10%	0.0	0.0	0.0	0.0	0.0	0.0

Only 0.5% of the estimations has an error between 5% and 10% for the rib flange. Within this range, the maximum percentage error was determined as 7%. Nevertheless, the vast

majority of estimates have less than a 3% error, as given in Table 5.2. Hence, the model gives outstanding results.

The model can also be examined for different cases with randomly selected test samples to get a better insight. For this reason, test samples can be divided into three different groups. These groups are created using the samples chosen:

- from the values of input variables (Test Group-1)
- within the range of input variables not introduced to the model before (Test Group-2)
- outside the range of input variables. (Test Group-3)

Test Group 1:

The first group, Test Group 1, is composed of the samples adopted from the values of the input variables. In fact, the samples were actually involved in evaluating the model's accuracy, as tabulated in Table 5.2.As tabulated in Table 5.3, it contains six samples with three internal rib configurations and a variety of thicknesses of the components.

Table 5.3 Test Group 1, the Samples from the Values of the Input Variables

Sample	Number of Internal Ribs	Skin Thickness [mm]	Rib Thickness [mm]	Spar Web Thickness [mm]	Spar Flange Thickness [mm]
1	2	0.51	0.51	3	1.5
2	2	1.27	2.03	3.5	3.5
3	3	2.03	0.51	2.5	1.5
4	3	1.27	0.81	1.5	2.5
5	4	0.81	1.27	2.5	2.5
6	4	2.03	0.81	1.5	3.5

The ANN outputs are given and compared with the FEA results in Table 5.4 for the samples selected from the values of the input variables. Correspondingly, the maximum total displacement of the horizontal stabilizer, the maximum von Mises stresses of each component, and the maximum axial stress on the flanges are presented. As seen from the table, the corresponding results are pretty similar to one another for each sample.

Table 5.4 Results of the Test Group 1

Sample	Source	Max Total Displacement [mm]	Max Von Mises Stress [MPa]			Max Axial Stress [MPa]	
			Skin	Rib	Spar Web	Rib Flange	Spar Flange
1	FEA	8.60	98.35	72.16	54.04	23.86	61.10
	ANN	8.62	98.50	72.34	54.23	24.12	61.52
2	FEA	3.60	40.16	29.41	26.10	8.22	30.10
	ANN	3.60	40.33	29.60	25.87	8.02	29.74
3	FEA	3.41	58.18	39.27	40.83	19.06	49.81
	ANN	3.39	58.33	39.92	40.64	18.75	49.38
4	FEA	4.41	60.62	42.91	38.70	15.05	45.12
	ANN	4.38	60.84	43.44	38.81	15.04	45.31
5	FEA	5.33	56.02	37.11	38.45	12.59	44.13
	ANN	5.33	56.68	37.66	38.62	12.58	44.23
6	FEA	2.96	43.91	31.05	28.75	12.04	33.51
	ANN	2.93	43.42	30.91	28.44	11.82	33.29

The percentage error of the ANN outputs based on the FEA results is presented in Table 5.5 for Test Group 1. The percentage errors obtained for this group are quite small, with a maximum calculated percentage error of 2.47%. Hence, it can be said that the ANN model performs admirably given the values of the input variables.

Table 5.5 The Percentage Error of the ANN Outputs for Test Group 1

Sample	Max Total Displacement, Error [%]	Max Von Mises Stress, Error [%]			Max Axial Stress, Error [%]	
		Skin	Rib	Spar Web	Rib Flange	Spar Flange
1	0.26	0.15	0.25	0.35	1.07	0.68
2	0.10	0.43	0.65	0.89	**2.47**	1.20
3	0.41	0.25	1.65	0.47	1.62	0.86
4	0.66	0.36	1.24	0.27	0.10	0.42
5	0.08	1.18	1.50	0.44	0.02	0.23
6	0.85	1.10	0.45	1.09	1.83	0.67

Test Group 2:

Table 5.6 lists the samples of Test Group 2. It is comprised of samples within the range of the input variables. However, the samples have not been introduced to the ANN model before.

Table 5.6 Test Group 2, Samples within the Range of Input Variables not Introduced to the Model Before

Sample	Number of Internal Ribs	Skin Thickness [mm]	Rib Thickness [mm]	Spar Web Thickness [mm]	Spar Flange Thickness [mm]
1	2	1.8	1.42	2.25	1.75
2	2	1.42	1.8	2.25	3.25
3	3	1.8	1.02	3.25	2.25
4	3	1.8	1.42	1.75	2.25
5	4	1.02	1.02	3.25	3.25
6	4	0.64	1.8	3.25	3.25

The group again includes six samples with three internal rib configurations and various thicknesses of the components. This test group will give an idea about the model's generalization capability since the model has not previously experienced the given inputs.

The ANN outputs and FEA results are given and compared in Table 5.7 for the samples within the range of the input variables not given to the ANN model before. The ANN outputs again seem fairly similar to the FEA results. It can be said that the model successfully predicts the maximum displacement of the stabilizer and the maximum von Mises and axial stresses on the components for this group. However, the percentage error of the model should be checked before the final decision is made.

Table 5.7 Results of Test Group 2

Sample	Source	Max Total Displacement [mm]	Max Von Mises Stress [MPa]			Max Axial Stress [MPa]	
			Skin	Rib	Spar Web	Rib Flange	Spar Flange
1	FEA	3.58	52.42	37.17	36.42	12.19	43.27
	ANN	3.62	52.68	37.32	36.70	12.24	43.59
2	FEA	3.63	44.13	32.27	28.67	9.14	33.29
	ANN	3.65	44.29	32.67	28.73	9.08	33.32
3	FEA	3.28	46.83	32.92	31.76	11.65	37.72
	ANN	3.31	46.56	32.76	31.58	11.26	37.56
4	FEA	3.48	49.37	34.71	34.50	11.56	40.53
	ANN	3.52	49.69	35.03	34.54	11.67	40.62
5	FEA	4.19	47.24	32.77	30.61	10.74	35.28
	ANN	4.16	47.36	33.12	30.44	10.49	35.14
6	FEA	5.24	46.48	29.51	32.65	10.24	36.79
	ANN	5.17	46.56	29.75	32.34	10.10	36.58

Table 5.8 exhibits the percentage error of the ANN outputs of Test Group 2. In comparison to Table 5.5, a similar error percentage range is observed, although there is a slight increase in the maximum error percentage. Therefore, the generalization capability of the ANN model appears to be remarkable in the range of inputs.

Table 5.8 The Percentage Error of the ANN Outputs for Test Group 2

Sample	Max Total Displacement, Error [%]	Max Von Mises Stress, Error [%]			Max Axial Stress, Error [%]	
		Skin	Rib	Spar Web	Rib Flange	Spar Flange
1	0.99	0.49	0.41	0.79	0.40	0.73
2	0.33	0.37	1.23	0.21	0.63	0.09
3	0.80	0.58	0.49	0.55	**3.37**	0.42
4	0.95	0.64	0.93	0.13	0.89	0.23
5	0.69	0.27	1.06	0.54	2.35	0.38
6	1.34	0.16	0.81	0.95	1.38	0.55

Test Group 3

The last test group, Test Group 3, is shown in Table 5.9. It includes the samples with the values outside the range of input variables. The values in bold in the table are outside the range. The extrapolation capability of the ANN model is evaluated through this test group. The ANN and FEA results are again presented and compared in Table 5.10.

Table 5.9 Test Group 3, the Samples with the Values outside the Range of Input Variables.

Sample	Number of Internal Ribs	Skin Thickness [mm]	Rib Thickness [mm]	Spar Web Thickness [mm]	Spar Flange Thickness [mm]
1	2	1.42	**2.54**	**3.75**	**5**
2	2	**2.54**	**0.41**	3.5	1.75
3	3	0.64	**0.41**	**4.5**	**4.5**
4	3	**2.29**	1.42	**4.5**	3
5	4	**2.54**	1.02	3.25	**4**
6	4	**0.41**	1.27	1.5	**4**

Table 5.10 Results of Test Group 3

Sample	Source	Max Total Displacement [mm]	Max Von Mises Stress [MPa]			Max Axial Stress [MPa]	
			Skin	Rib	Spar Web	Rib Flange	Spar Flange
1	**FEA**	2.94	29.16	19.94	19.46	5.15	22.11
	ANN	2.95	30.47	21.86	17.59	4.71	20.02
2	**FEA**	2.75	49.20	32.92	33.83	18.56	41.65
	ANN	2.48	49.07	33.94	33.32	17.36	41.31
3	**FEA**	4.90	58.10	45.30	26.88	16.45	29.75
	ANN	4.63	61.05	44.09	26.52	16.31	29.91
4	**FEA**	2.51	34.85	25.03	23.72	8.24	28.21
	ANN	2.28	33.17	24.06	22.63	7.84	27.49
5	**FEA**	2.29	33.20	23.50	22.20	8.75	26.43
	ANN	1.90	30.69	22.37	20.12	8.03	24.13
6	**FEA**	6.50	54.10	34.42	35.60	11.71	39.26
	ANN	6.50	54.41	34.27	35.52	11.97	38.85

As seen in Table 5.10, the results in this group are not as accurate as the previous groups. In addition, the percentage error due to the difference between the ANN outputs and the FEA results is presented for Test Group 3 in Table 5.11.

Table 5.11 The Percentage Error of the ANN Outputs for Test Group 3

| Sample | Max Total Displacement, Error [%] | Max Von Mises Stress, Error [%] | | | Max Axial Stress, Error [%] | |
		Skin	Rib	Spar Web	Rib Flange	Spar Flange
1	0.18	4.51	9.64	9.59	8.51	9.44
2	9.67	0.26	3.09	1.50	6.49	0.81
3	5.48	5.08	2.66	1.35	0.88	0.55
4	9.21	4.82	3.88	4.60	4.86	2.58
5	**17.17**	7.54	4.82	9.37	8.20	8.70
6	0.05	0.58	0.45	0.23	2.20	1.05

The table reveals that the percentage errors are much higher than both previous groups, with a maximum percentage error of 17.17%. Unsurprisingly, the extrapolation capability of the ANN model is not as satisfactory as the generalization capability between the input limits.

In the following sections, the effect of decreasing the number of input data using Hammersley sampling will be studied. First, the data distribution percentiles according to the estimation errors will be given for the entire data. Then, the models will be examined with Test Group-1 since it gives the most accurate results among test groups.

5.4.2. ANN Generation with 75% of the Original Input Data

The input data is reduced to 75% of the original input data through Hammersley sampling in HyperStudy. Then, the ANN model is generated using this data. The correlation coefficient of the model was determined as 0.99299. Moreover, the data distribution percentile is exhibited in Table 5.12 according to the percentage error for the reduced input data. The data distribution of less than 3% error decreases slightly compared to

Table 5.2. Although the maximum percentage error of the model was determined as 9.9%, most estimates still have less than a 3% error.

Table 5.12 Accuracy of the ANN model with 75% of the Initial Input Data

| Percentage Error | Data Distribution Percentile [%] | | | | | |
| | Max Total Displacement | Max Von Mises Stress | | | Max Axial Stress | |
		Skin	Rib	Spar Web	Rib Flange	Spar Flange
< 3%	99.0	98.6	94.9	99.6	91.3	99.7
3% - 5%	1.0	1.4	4.8	0.4	7.7	0.3
5% - 10%	0.0	0.1	0.3	0.0	1.0	0.0
> 10%	0.0	0.0	0.0	0.0	0.0	0.0

Table 5.13 compares the FEA results and ANN model with 75% of the original data for Test Group 1. It is clear that the model gives similar results to the FEA results.

Table 5.13 Results of the ANN with 75% of the Input Data

| Sample | Source | Max Total Displacement [mm] | Max Von Mises Stress [MPa] | | | Max Axial Stress [MPa] | |
			Skin	Rib	Spar Web	Rib Flange	Spar Flange
1	FEA	8.60	98.35	72.16	54.04	23.86	61.10
	ANN	8.62	98.15	71.87	53.87	24.26	61.33
2	FEA	3.60	40.16	29.41	26.10	8.22	30.10
	ANN	3.64	40.24	29.62	25.43	7.97	29.50
3	FEA	3.41	58.18	39.27	40.83	19.06	49.81
	ANN	3.39	58.46	40.02	40.80	18.67	49.52
4	FEA	4.41	60.62	42.91	38.70	15.05	45.12
	ANN	4.37	60.01	42.12	38.82	14.78	45.31
5	FEA	5.33	56.02	37.11	38.45	12.59	44.13
	ANN	5.31	56.33	37.19	38.69	12.58	44.35
6	FEA	2.96	43.91	31.05	28.75	12.04	33.51
	ANN	2.92	43.63	30.63	28.73	11.72	33.84

The percentage error of the model is provided in Table 5.14. There is a slight increase in percentage errors for most estimations in comparison to Table 5.5. The maximum percentage error is obtained as 3.10% which is a bit higher than that of the original ANN model. Nevertheless, the model results are highly promising.

Table 5.14 The Percentage Error of the ANN with 75% of the Input Data

Sample	Max Total Displacement, Error [%]	Max Von Mises Stress, Error [%]			Max Axial Stress, Error [%]	
		Skin	Rib	Spar Web	Rib Flange	Spar Flange
1	0.19	0.20	0.41	0.31	1.68	0.38
2	1.02	0.20	0.70	2.56	**3.10**	1.97
3	0.57	0.47	1.90	0.08	2.05	0.58
4	0.85	1.01	1.85	0.31	1.80	0.43
5	0.24	0.54	0.22	0.62	0.05	0.51
6	1.30	0.62	1.34	0.09	2.68	0.97

5.4.3. ANN Generation with 50% of the Original Input Data

This time, the input data is reduced to 50% of the original input data through Hammersley sampling in HyperStudy. The ANN model is reconstructed using this data. The correlation coefficient of the model was determined as 0.98891. It is the lowest correlation value obtained among ANN models. Moreover, the data distribution percentile according to the percentage error is given in Table 5.15 for the reduced input data.

Table 5.15 Accuracy of the ANN model with 50% of the Initial Input Data

Percentage Error	Data Distribution Percentile [%]					
	Max Total Displacement	Max Von Mises Stress			Max Axial Stress	
		Skin	Rib	Spar Web	Rib Flange	Spar Flange
< 3%	98.4	96.6	92.2	98.3	83.0	98.2
3% - 5%	1.6	2.4	7.3	1.5	13.8	1.6
5% - 10%	0.0	1.1	0.5	0.2	3.1	0.2
> 10%	0.0	0.0	0.0	0.0	0.1	0.0

Compared to Table 5.2 and Table 5.12, the overall percentage error has increased. Moreover, estimates with an error of more than 10% were obtained. As given in the table, the estimations for the ribs and rib flanges are not as accurate as the other components. Since the change in the number of internal ribs is discrete, not continuous, the stress on the rib component varies much and is hard to predict with inadequate data. That is the reason why the estimation error of the rib components is greater than others.

The FEA and ANN model results with 50% of the original data are given in Table 5.16 for Test Group 1. The table shows that the ANN results differ from the FEA results for some values.

Table 5.16 Results of the ANN with 50% of the Input Data

Sample	Source	Max Total Displacement [mm]	Max Von Mises Stress [MPa]			Max Axial Stress [MPa]	
			Skin	Rib	Spar Web	Rib Flange	Spar Flange
1	FEA	8.60	98.35	72.16	54.04	23.86	61.10
	ANN	8.43	95.46	69.32	53.68	23.74	61.10
2	FEA	3.60	40.16	29.41	26.10	8.22	30.10
	ANN	3.53	38.57	27.81	25.27	7.84	29.68
3	FEA	3.41	58.18	39.27	40.83	19.06	49.81
	ANN	3.35	58.03	39.46	40.33	18.76	49.26
4	FEA	4.41	60.62	42.91	38.70	15.05	45.12
	ANN	4.43	60.52	42.37	38.92	15.27	45.15
5	FEA	5.33	56.02	37.11	38.45	12.59	44.13
	ANN	5.29	56.22	37.59	37.97	12.57	43.43
6	FEA	2.96	43.91	31.05	28.75	12.04	33.51
	ANN	2.95	43.60	30.90	28.93	12.32	34.13

The percentage error between the ANN and FEA results is given in Table 5.17. Although the percentage errors of some samples are small, higher error percentages occur in this model. In comparison to Table 5.5 and Table 5.14, the ANN model starts to make

estimations with an error of more than 5%. Therefore, the model with 50% reduced input data is definitely not as reliable as the other models generated previously.

Table 5.17 The Percentage Error of the ANN with 50% of the Input Data

Sample	Max Total Displacement, Error [%]	Max Von Mises Stress, Error [%]			Max Axial Stress, Error [%]	
		Skin	Rib	Spar Web	Rib Flange	Spar Flange
1	1.99	2.94	3.94	0.66	0.50	0.01
2	1.89	3.97	**5.46**	3.18	4.62	1.39
3	1.69	0.26	0.48	1.24	1.58	1.12
4	0.50	0.16	1.27	0.57	1.41	0.06
5	0.78	0.35	1.29	1.25	0.13	1.57
6	0.41	0.70	0.47	0.62	2.30	1.83

6. CONCLUSION

In this thesis, ANNs have been utilized to determine the static structural characteristics of the horizontal stabilizer of a helicopter. The database required to train the model was provided by the FEA of the horizontal stabilizer under the aerodynamic pressure load. Correspondingly, 1875 analyses were performed for different design variables, namely, the number of internal ribs, the skin thickness, the rib thickness, the spar web thickness, and the spar flange thickness. These design variables are the inputs for the tool developed to determine the maximum total displacement of the wing, the maximum von Mises stresses on the skin, rib, and spar web, and the maximum axial stresses on the rib flange and the spar flanges.

Firstly, the model with the full factorial design (i.e., including 1875 analyses) was examined. Most of the model results had an error of less than 3%, and the correlation between the output and the target was relatively high. In addition, different cases were created to test randomly selected samples. The model gave excellent results in the range of inputs. Therefore, the generalization capability of the model was considered remarkable. However, the accuracy of the model results dropped much outside the range of inputs. Hence, the extrapolation capability of the model was not evaluated as satisfactory as the generalization capability.

Then, the effect of decreasing the number of input data using Hammersley sampling was studied. The input data is first reduced to 75% of the original input data through Hammersley sampling. Due to the excellent uniformity properties of Hammersley sampling, the model's accuracy has not decreased much. Afterward, Hammersley sampling reduces the input data to 50% of the original input data. Although some estimates were highly accurate, the model gave some estimates with an error of even more than 10%. Unfortunately, the model's reliability decreased.

In conclusion, the ANN-based design tool developed in this study can be considered a powerful tool for predicting the desired structural characteristics of the horizontal

stabilizer. Moreover, it was observed that it is possible to decrease the data required for the ANN model using the Hammersley sampling methodology.

6.1. Future Works

The horizontal stabilizer model can be further detailed to obtain more realistic results. Lightening holes can be added to the ribs and spars. The stringers can also be modelled as additional stiffeners. Moreover, the thesis involved only the static analysis of the horizontal stabilizer. Therefore, it is also possible to perform the stabilizer's buckling and dynamic analysis. The component materials can be entered into the tool as inputs. Hence, different material selections can also be examined. Furthermore, aluminum materials used for the components can be replaced with composite materials. The study includes only the forward cruise flight condition to which stabilizers are typically configured. Therefore, different load cases can be created by considering different flight conditions, such as maneuvers. As mentioned before, the database required to train the model was provided by the FEA of the horizontal stabilizer. Therefore, the FEM of the stabilizer can be calibrated using the test data to obtain more accurate results. Lastly, the database can be generated employing the test data if possible.

7. REFERENCES

[1] A. Fouto, M. A. Gomes, and A. Suleman, "Multidisciplinary Optimization Strategies Using Evolutionary Algorithms with Application to Aircraft Design," in *50th AIAA/ASME/ASCE/AHS/ASC Structures, Structural Dynamics, and Materials Conference*, May 2009. doi: 10.2514/6.2009-2205.

[2] F. Yildirim Dalkiran and M. Toraman, "Predicting thrust of aircraft using artificial neural networks," *Aircraft Engineering and Aerospace Technology*, vol. 93, no. 1, pp. 35–41, Feb. 2021, doi: 10.1108/AEAT-05-2020-0089.

[3] H. Salehi and R. Burgueño, "Emerging artificial intelligence methods in structural engineering," *Eng Struct*, vol. 171, pp. 170–189, Sep. 2018, doi: 10.1016/j.engstruct.2018.05.084.

[4] S. B. Cooper and D. DiMaio, "Static load estimation using artificial neural network: Application on a wing rib," *Advances in Engineering Software*, vol. 125, pp. 113–125, Nov. 2018, doi: 10.1016/j.advengsoft.2018.01.007.

[5] S. H. Jeong, K. B. Lee, J. H. Ham, J. H. Kim, and J. Y. Cho, "Estimation of Maximum Strains and Loads in Aircraft Landing Using Artificial Neural Network," *International Journal of Aeronautical and Space Sciences*, vol. 21, no. 1, pp. 117–132, Mar. 2020, doi: 10.1007/s42405-019-00204-2.

[6] J. Gómez-Escalonilla, J. García, and J. I. Armijo, "Strain predictions using Artificial Neural Networks for a full-scale fatigue monitoring system," 2009.

[7] A. Yildirim, A. A. Akay, H. Gulasik, E. Gurses, D. Coker, and A. Kayran, "Development of Bolted Flange Design Tool Based on Finite Element Analysis and Artificial Neural Network," 2015.

[8] M. T. Ozkan and F. Erdemir, "Determination of theoretical stress concentration factor for circular/elliptical holes with reinforcement using analytical, finite element method and artificial neural network techniques," *Neural Comput Appl*, vol. 33, no. 19, pp. 12641–12659, Oct. 2021, doi: 10.1007/s00521-021-05914-x.

[9] J. P. A. Ribeiro, L. F. F. Gomes, and S. M. O. Tavares, "Artificial Neural Networks Applied in Mechanical Structural Design," *Journal of Computation and Artificial Intelligence in Mechanics and Biomechanics*, vol. 1, no. 1, pp. 14–21, 2021, doi: 10.5281/zenodo.4669797.

[10] J. P. Ribeiro, S. M. Tavares, and M. Parente, "Stress–strain evaluation of structural parts using artificial neural networks," *Proceedings of the Institution of Mechanical Engineers, Part L: Journal of Materials: Design and Applications*, vol. 235, no. 6, pp. 1271–1286, Jun. 2021, doi: 10.1177/1464420721992445.

[11] S. Rusia and K. K. Pathak, "Application of Artificial Neural Network for Analysis of Triangular Plate with Hole Considering Different Geometrical and Loading Parameters," *Open Journal of Civil Engineering*, vol. 06, no. 01, pp. 31–41, 2016, doi: 10.4236/ojce.2016.61004.

[12] S. Selvakumar, K. P. Arulshri, K. P. Padmanaban, and K. S. K. Sasikumar, "Design and optimization of machining fixture layout using ANN and DOE," *The International Journal of Advanced Manufacturing Technology*, vol. 65, no. 9–12, pp. 1573–1586, Apr. 2013, doi: 10.1007/s00170-012-4281-2.

[13] Ž. Ćojbašić *et al.*, "A Real Time Neural Network Based Finite Element Analysis of Shell Structure," 2014.

[14] E. Tosun and A. Çalık, "Failure load prediction of single lap adhesive joints using artificial neural networks," *Alexandria Engineering Journal*, vol. 55, no. 2, pp. 1341–1346, Jun. 2016, doi: 10.1016/j.aej.2016.04.029.

[15] B. Sidda Reddy, J. Suresh Kumar, K. Vijaya, and K. Reddy, "Prediction of Deflection and Stresses of Laminated Composite Plate with an Artificial Neural Network Aid," 2013.

[16] M. Das, S. Sahu, and D. R. Parhi, "Composite materials and their damage detection using AI techniques for aerospace application: A brief review," *Mater Today Proc*, vol. 44, pp. 955–960, 2021, doi: 10.1016/j.matpr.2020.11.005.

[17] E. M. Bezerra, A. C. Ancelotti, L. C. Pardini, J. A. F. F. Rocco, K. Iha, and C. H. C. Ribeiro, "Artificial neural networks applied to epoxy composites reinforced with carbon and E-glass fibers: Analysis of the shear mechanical properties,"

Materials Science and Engineering: A, vol. 464, no. 1–2, pp. 177–185, Aug. 2007, doi: 10.1016/j.msea.2007.01.131.

[18]   Z. Zhang and K. Friedrich, "Artificial neural networks applied to polymer composites: a review," *Compos Sci Technol*, vol. 63, no. 14, pp. 2029–2044, Nov. 2003, doi: 10.1016/S0266-3538(03)00106-4.

[19]   M. R. S. Reddy, B. S. Reddy, V. N. Reddy, and S. Sreenivasulu, "Prediction of Natural Frequency of Laminated Composite Plates Using Artificial Neural Networks," *Engineering*, vol. 04, no. 06, pp. 329–337, 2012, doi: 10.4236/eng.2012.46043.

[20]   A. Reddy, B. Reddy, and K. Reddy, "Application of design of experiments and artificial neural networks for stacking sequence optimizations of laminated composite plates," *International Journal of Engineering, Science and Technology*, vol. 3, no. 6, pp. 295–310, Jan. 2011, doi: 10.4314/ijest.v3i6.24.

[21]   F. P. Beer, *Mechanics of Materials*, 6th Edition. McGraw-Hill Higher Education, 2009.

[22]   Z. Sun, Z. Lei, J. Zou, R. Bai, H. Jiang, and C. Yan, "Prediction of failure behavior of composite hat-stiffened panels under in-plane shear using artificial neural network," *Compos Struct*, vol. 272, p. 114238, Sep. 2021, doi: 10.1016/j.compstruct.2021.114238.

[23]   S. Kumar, R. Kumar, S. Mandal, and A. K. Rahul, "The Prediction of Buckling Load of Laminated Composite Hat-Stiffened Panels Under Compressive Loading by Using of Neural Networks," *The Open Civil Engineering Journal*, vol. 12, no. 1, pp. 468–480, Dec. 2018, doi: 10.2174/1874149501812010468.

[24]   P. E. Nicholas, K. P. Padmanaban, D. Vasudevan, and I. J. Selvaraj, "Neural network based buckling strength prediction of laminated composite plate with central cutout," in *Applied Mechanics and Materials*, 2014, vol. 592–594, pp. 560–564. doi: 10.4028/www.scientific.net/AMM.592-594.560.

[25]   S. Guzel and E. Gurses, "Determination of the 1st Buckling and Collapse Loads for Integrally Stiffened Panels by Artificial Neural Network and Design of Experiment Methodology," *IOP Conf Ser Mater Sci Eng*, vol. 1024, no. 1, p. 012080, Jan. 2021, doi: 10.1088/1757-899X/1024/1/012080.

[26] R. M. Paiva, A. R. D. Carvalho, C. Crawford, and A. Suleman, "Comparison of Surrogate Models in a Multidisciplinary Optimization Framework for Wing Design," *AIAA Journal*, vol. 48, no. 5, pp. 995–1006, May 2010, doi: 10.2514/1.45790.

[27] N. R. Secco and B. S. de Mattos, "Artificial neural networks to predict aerodynamic coefficients of transport airplanes," *Aircraft Engineering and Aerospace Technology*, vol. 89, no. 2, pp. 211–230, Mar. 2017, doi: 10.1108/AEAT-05-2014-0069.

[28] M. Santos, B. Mattos, and R. Girardi, "Aerodynamic Coefficient Prediction of Airfoils Using Neural Networks," in *46th AIAA Aerospace Sciences Meeting and Exhibit*, Jan. 2008. doi: 10.2514/6.2008-887.

[29] D. Graupe, *Principles of Artificial Neural Networks*, vol. 6. WORLD SCIENTIFIC, 2007. doi: 10.1142/6429.

[30] I. N. da Silva, D. Hernane Spatti, R. Andrade Flauzino, L. H. B. Liboni, and S. F. dos Reis Alves, *Artificial Neural Networks: A Practical Course*. Cham: Springer International Publishing, 2017. doi: 10.1007/978-3-319-43162-8.

[31] S. Susheel and P. Kode, "Conversion of Neural Network Models to State-Space Models for Model-Based Control Design," The University of Alabama in Huntsville, 2015.

[32] S. S. Haykin, *Neural Networks and Learning Machines*. Prentice Hall/Pearson, 2009.

[33] D. Anderson and G. Mcneill, "Artificial Neural Networks Technology," 1992.

[34] I. A. Basheer and M. Hajmeer, "Artificial neural networks: fundamentals, computing, design, and application," *J Microbiol Methods*, vol. 43, no. 1, pp. 3–31, Dec. 2000, doi: 10.1016/S0167-7012(00)00201-3.

[35] S. Sharma, S. Sharma, and A. Athaiya, "Activation Functions in Neural Networks," *International Journal of Engineering Applied Sciences and Technology*, vol. 04, no. 12, pp. 310–316, May 2020, doi: 10.33564/IJEAST.2020.v04i12.054.

[36] I. Goodfellow, Y. Bengio, and A. Courville, *Deep Learning*. The MIT Press, 2016.

[37] M. T. Hagan, H. B. Demuth, M. H. Beale, and O. de Jesús, *Neural Network Design*, 2nd ed. Boston: PWS publishing company, 1996.

[38] S.-H. Han, K. W. Kim, S. Kim, and Y. C. Youn, "Artificial Neural Network: Understanding the Basic Concepts without Mathematics," *Dement Neurocogn Disord*, vol. 17, no. 3, p. 83, 2018, doi: 10.12779/dnd.2018.17.3.83.

[39] R. Alejo, J. M. Sotoca, V. García, and R. M. Valdovinos, "Back Propagation with Balanced MSE Cost Function and Nearest Neighbor Editing for Handling Class Overlap and Class Imbalance," 2011, pp. 199–206. doi: 10.1007/978-3-642-21501-8_25.

[40] S. Ruder, "An overview of gradient descent optimization algorithms," Sep. 2016.

[41] M. A. Costa, A. de P. Braga, and B. R. de Menezes, "Improving generalization of MLPs with sliding mode control and the Levenberg–Marquardt algorithm," *Neurocomputing*, vol. 70, no. 7–9, pp. 1342–1347, Mar. 2007, doi: 10.1016/j.neucom.2006.09.003.

[42] D. P. Kingma and J. Ba, "Adam: A Method for Stochastic Optimization," Dec. 2014.

[43] A. Giunta, S. Wojtkiewicz, and M. Eldred, "Overview of Modern Design of Experiments Methods for Computational Simulations (Invited)," in *41st Aerospace Sciences Meeting and Exhibit*, Jan. 2003. doi: 10.2514/6.2003-649.

[44] U. M. Diwekar and J. R. Kalagnanam, "Efficient sampling technique for optimization under uncertainty," *AIChE Journal*, vol. 43, no. 2, pp. 440–447, Feb. 1997, doi: 10.1002/aic.690430217.

[45] T.-T. Wong, W.-S. Luk, and P.-A. Heng, "Sampling with Hammersley and Halton Points," *Journal of Graphics Tools*, vol. 2, no. 2, pp. 9–24, Jan. 1997, doi: 10.1080/10867651.1997.10487471.

[46] N. Dige and U. Diwekar, "Efficient sampling algorithm for large-scale optimization under uncertainty problems," *Comput Chem Eng*, vol. 115, pp. 431–454, Jul. 2018, doi: 10.1016/j.compchemeng.2018.05.007.

[47] W. J. Wagtendonk, *Principles of Helicopter Flight*, 2nd Edition. Newcastle, Washington: Aviation Supplies & Academics, Inc., 2006.

[48] R. W. Prouty, *Helicopter Performance, Stability, and Control*. Malabar, Florida: Krieger Publishing Company, 1995.

[49] J. Roskam, *Airplane Design Part III: Layout Design of Cockpit, Fuselage, Wing and Empennage: Cutaways and Inboard Profiles*. DARcorporation, 2002.

[50] J. D. Anderson, *Fundamentals of Aerodynamics*, 5th edition. McGraw-Hill, 2010.

[51] W. J. Wagtendonk, *Principles of Helicopter Flight*, 2nd Edition. Aviation Supplies & Academics, Inc., 2006.

[52] "Ansys® Fluent ver. 22.2." Ansys, Inc., Canonsburg, Pennsylvania, United States.

[53] D. Schulze, "Far field boundary conditions based on characteristic and bicharacteristic theory applied to transonic flows," in *Fourteenth International Conference on Numerical Methods in Fluid Dynamics*, Berlin, Heidelberg: Springer Berlin Heidelberg, 1995, pp. 211–215. doi: 10.1007/3-540-59280-6_124.

[54] F. Palacios *et al.*, "Stanford University Unstructured (SU2): Analysis and Design Technology for Turbulent Flows," in *52nd Aerospace Sciences Meeting*, Jan. 2014. doi: 10.2514/6.2014-0243.

[55] "Tecplot 360 2013 R1." Vela Software, Bellevue, Washington.

[56] "HyperWorks ver. 2019.1." Altair Engineering, Inc., Troy MI, United States.

[57] T. Dursun and C. Soutis, "Recent developments in advanced aircraft aluminium alloys," *Materials & Design (1980-2015)*, vol. 56, pp. 862–871, Apr. 2014, doi: 10.1016/j.matdes.2013.12.002.

[58] L. Zhu, N. Li, and P. R. N. Childs, "Light-weighting in aerospace component and system design," *Propulsion and Power Research*, vol. 7, no. 2, pp. 103–119, Jun. 2018, doi: 10.1016/j.jppr.2018.04.001.

[59] M. C.-Y. Niu, *Airframe Structural Design: Practical Design Information and Data on Aircraft Structures*, 2nd Edition. Conmilit Press, 1988.

[60] *Metallic materials properties development and standardization (MMPDS): MMPDS-08*. Washington, D.C.: Battelle Memorial Institute; United States Federal Aviation Administration, 2013.

[61] M. C.-Y. Niu, *Airframe Stress Analysis and Sizing*, 2nd Edition. Hong Kong Conmilit Press, 1999.

[62] P. Kelly, *Solid Mechanics Part I: An Introduction to Solid Mechanics*. The University of Auckland, 2013. [Online]. Available: homepages.engineering.auckland.ac.nz/~pkel015/SolidMechanicsBooks/index.html

[63] G. Krauss, J. I. Kindangen, and P. Depecker, "Using artificial neural networks to predict interior velocity coefficients," *Build Environ*, vol. 32, no. 4, pp. 295–303, Jul. 1997, doi: 10.1016/S0360-1323(96)00059-5.